nature chemistry

Article

https://doi.org/10.1038/s41557-023-01305-y

Stabilizing Au^{2+} in a mixed-valence 3D halide perovskite

Received: 3 October 2022

Accepted: 24 July 2023

Published online: 28 August 2023

Check for updates

Kurt P. Lindquist[1], Armin Eghdami[2], Christina R. Deschene[1], Alexander J. Heyer[1], Jiajia Wen[3], Alexander G. Smith[2], Edward I. Solomon[1,4], Young S. Lee[3,5], Jeffrey B. Neaton[2,6,7], Dominic H. Ryan[8] & Hemamala I. Karunadasa[1,3]

Although Cu^{2+} is ubiquitous, the relativistic destabilization of the 5d orbitals makes the isoelectronic Au^{2+} exceedingly rare, typically stabilized only through Au–Au bonding or by using redox non-innocent ligands. Here we report the perovskite $Cs_4Au^{II}Au^{III}{}_2Cl_{12}$, an extended solid with mononuclear Au^{2+} sites, which is stable to ambient conditions and characterized by single-crystal X-ray diffraction. The 2+ oxidation state of Au was assigned using ^{197}Au Mössbauer spectroscopy, electron paramagnetic resonance, and magnetic susceptibility measurements, with comparison to paramagnetic and diamagnetic analogues with Cu^{2+} and Pd^{2+}, respectively, as well as to density functional theory calculations. This gold perovskite offers an opportunity to study the optical and electronic transport of the uncommon $Au^{2+/3+}$ mixed-valence state and the characteristics of the elusive Au^{2+} ion coordinated to simple ligands. Compared with the perovskite $Cs_2Au^{I}Au^{III}Cl_6$, which has been studied since the 1920s, $Cs_4Au^{II}Au^{III}{}_2Cl_{12}$ exhibits a 0.7 eV reduction in optical absorption onset and a 10^3-fold increase in electronic conductivity.

Many of the peculiar properties of Au, including the golden lustre of its elemental form, stem from relativistic effects[1]. The relativistic destabilization of the 5d orbitals also makes $5d^9$ Au^{2+} unfavourable, in contrast to the ubiquitous and isoelectronic $3d^9$ Cu^{2+} ion. Thus, mononuclear Au^{2+} species, proposed as transient intermediates in catalytic reactions[2], remain elusive[3]. In discrete molecules, mononuclear Au^{2+} centres have been realized with some participation of the ligand. For example, redox non-innocent dithiolenes flank formally Au^{2+} centres[4], where the spin density is partially on the coordinating S atoms[5], cyclic thioethers, which calculations suggest are also not redox-innocent[6–8], have afforded a few mononuclear Au^{2+} molecules[8,9], and Au^{2+} has been stabilized in a tetraphenylporphyrin macrocycle, where electron paramagnetic resonance (EPR) spectroscopy evidence suggests some spin delocalization over the ligand[10]. Dimers with Au–Au bonds more commonly stabilize the formal Au^{2+} oxidation state in both molecules[11,12] and in extended solids such as in $AuSO_4$ (ref. 13), where the unpaired 5d electron in each metal is paired and stabilized in a bonding molecular orbital. In the absence of redox-active ligands and Au–Au bonds, the very rare examples of Au^{2+} in extended solids require extreme conditions (GPa-scale pressures)[14,15] or F-based (for example, F^-, HF, SbF_6^-, SbF_5•SbF_6^-) or Xe ligands[16–19] to form exotic coordination solids using superacids (anhydrous HF acidified with SbF_5) through manipulations in metal/Teflon-lined vacuum lines. These solids are unstable to hydrolysis from atmospheric moisture and often are stable only at low temperatures or under inert atmosphere.

[1]Department of Chemistry, Stanford University, Stanford, CA, USA. [2]Department of Physics, University of California Berkeley, Berkeley, CA, USA. [3]Stanford Institute for Materials and Energy Sciences, SLAC National Accelerator Laboratory, Menlo Park, CA, USA. [4]Stanford Synchrotron Radiation Lightsource, SLAC National Accelerator Laboratory, Stanford University, Menlo Park, CA, USA. [5]Department of Applied Physics, Stanford University, Stanford, CA, USA. [6]Materials Sciences Division, Lawrence Berkeley National Laboratory, Berkeley, CA, USA. [7]Kavli Energy NanoSciences Institute at Berkeley, Berkeley, CA, USA. [8]Physics Department and Centre for the Physics of Materials, McGill University, Montreal, Quebec, Canada. e-mail: hemamala@stanford.edu

https://doi.org/10.1038/s41557-023-01305-y

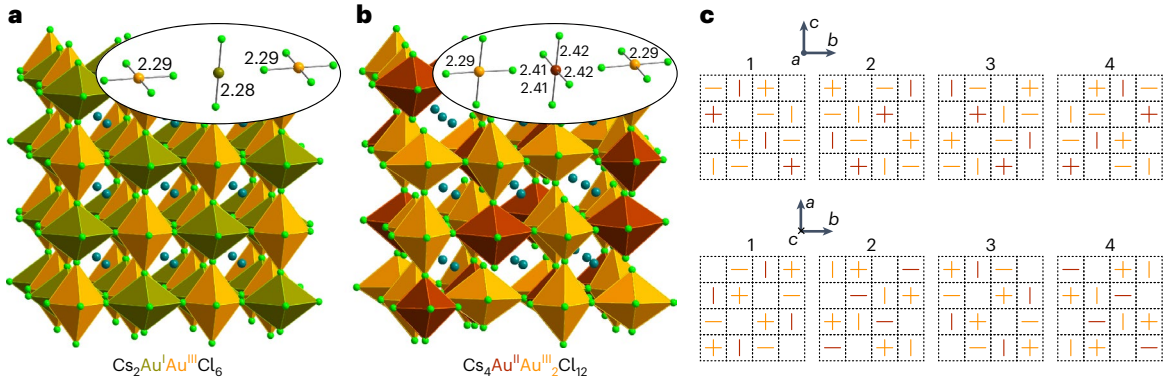

Fig. 1 | Single-crystal XRD structures. a, The known $Cs_2Au^IAu^{III}Cl_6$ (ref. 24). **b**, The new $Cs_4Au^{II}Au^{III}{}_2Cl_{12}$ (**Au_Cl**). The structure of **Au_Cl** contains trimers of mutually orthogonal elongated Au–Cl octahedra. The trimers are separated by vacancies at the octahedral metal site and each trimer contains one Au^{2+} and two Au^{3+}. Insets show the local coordination, with bond lengths in Å, highlighting the longer bond lengths for Au^{2+} compared with those for Au^{3+}. Dark-green, burnt-red and gold polyhedra represent Au^ICl_6, $Au^{II}Cl_6$ and $Au^{III}Cl_6$, respectively. Turquoise and light-green spheres represent Cs and Cl atoms, respectively. Whereas $Cs_4Pd^{II}Au^{III}{}_2Cl_{12}$ (**Pd_Cl**; Extended Data Fig. 1) is isostructural with **Au_Cl**, $Cs_4Cu^{II}Au^{III}{}_2Cl_{12}$ (**Cu_Cl**; Extended Data Fig. 2) is similar in structure but with a different B-site ordering. **c**, 2D representations of the **Au_Cl** structure where the short, equatorial bonds of the axially elongated $Au^{III}Cl_6$ and $Au^{II}Cl_6$ octahedra are represented by gold and burnt-red lines, respectively. Equatorial bonds perpendicular to the plane are not drawn. The numbers represent the layer stacking sequence along the *a* axis (top) and the *c* axis (bottom).

Halide perovskites hold an important place in the history of gold chemistry. These ionic solids contain metal–halide octahedra that share corners to form a three-dimensional (3D) anionic framework, with monovalent cations residing between the octahedra. With the formula $A^IB^{II}X_3$ (X, halide), many divalent metals occupy the octahedral B sites. Intriguingly, Cu^{2+} and Ag^{2+} fluorides adopt a 3D perovskite structure with axially elongated octahedra due to the Jahn–Teller distortion of the d^9 metals[20,21], although the isoelectronic Au^{2+} halide perovskites are unknown. The opaque black perovskite $CsAuX_3$ was first described by Horace Wells in 1922 (ref. 22). Despite the formal Au^{2+} in the formula, this material is more accurately described as the double perovskite $Cs_2Au^IAu^{III}X_6$ (ref. 23), as crystallographically characterized by Linus Pauling in 1938 (ref. 24) and later refined further[25]. In $Cs_2Au^IAu^{III}X_6$, Au cations, in the common oxidation states of 1+ and 3+, alternate in the B sites in a chequerboard pattern (Fig. 1a). Upon compression above 11 GPa, the linear and square-planar coordination spheres of the $5d^{10}$ Au^{1+} and $5d^8$ Au^{3+}, respectively, are thought to become equivalent, resulting in the transient generation of $5d^9$ Au^{2+} sites in the perovskite and complete electronic delocalization between the metals[14,15]. The non-stoichiometric compound $CsAu_{0.6}Br_{2.6}$, with an average valence of 2.67 for the Au centres, was deduced to contain some Au^{2+} based on a broad isotropic EPR signal, and was ascribed to be a cubic perovskite with equivalent $AuBr_6$ octahedra based on powder X-ray diffraction (XRD) data[26–28]. A detailed study of the complex Cs–Au–Br ternary phase, featuring substantial deviations from the structure of $Cs_4Au^{II}Au^{III}{}_2Cl_{12}$, will be reported in a future publication.

The magnetic $3d^9$ Cu analogues $Cs_4Cu^{II}Au^{III}{}_2X_{12}$ ($X = Cl^-, Br^-$) and diamagnetic $4d^8$ Pd analogues $Cs_4Pd^{II}Au^{III}{}_2X_{12}$ ($X = Cl^-, Br^-, I^-$) have been subjected to a handful of studies since 1922, although the structural investigations did not capture the B-site ordering revealed through the single-crystal XRD studies described here (in Supplementary Information, see 'Prior work on $Cs_4CuAu_2Cl_{12}$ (**Cu_Cl**) and $Cs_4PdAu_2Cl_{12}$ (**Pd_Cl**)'). These perovskites serve as controls for better understanding the properties inherent to unpaired 5d electrons in Au^{2+}.

Results and discussion

Synthesis and structure

The dark-green solid $Cs_4Au^{II}Au^{III}{}_2Cl_{12}$ (or $Cs_4Au^{II}Au^{III}{}_2\square Cl_{12}$; **Au_Cl**; Fig. 2) was synthesized by combining CsCl and $AuCl_3$ in 6 M aqueous HCl under ambient conditions, and single crystals could be formed by cooling the solution from 110 °C to room temperature (25 °C).

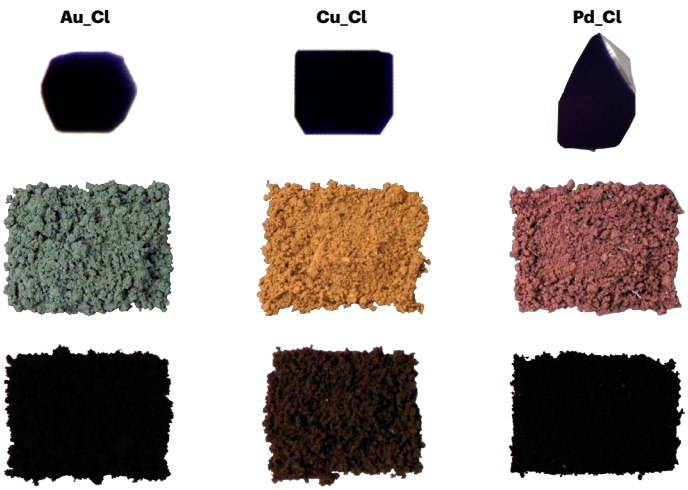

Fig. 2 | Photographs of the $Cs_4M^{II}Au^{III}{}_2Cl_{12}$ perovskites: M = Au^{2+} (Au_Cl), Cu^{2+} (Cu_Cl), and Pd^{2+} (Pd_Cl). Top row, single crystals; middle row, powders on a black background for enhanced contrast; bottom row, powders on a white background.

The reduction of Au^{3+} to Au^{2+} occurred spontaneously in HCl, though a mild reductant, such as ascorbic acid, was required to produce phase-pure **Au_Cl** (for details, see Methods). In contrast, synthesis in 70% (v/v) ethanol yielded **Au_Cl** without added reductant, although in low yield. The detection of Cl_2 in the ethanol solution confirmed the oxidation of Cl^- in reactions without another added reductant (Supplementary Fig. 1). All measurements, except otherwise noted, were performed on the **Au_Cl** powder synthesized in HCl. The reaction in HCl probably occurs through a solvent-mediated solid-to-solid conversion, through the solid intermediate $CsAuCl_4$, which forms upon combining CsCl and $AuCl_3$ in HCl, due to the following observations: first, solid $CsAuCl_4$ must be present in the reaction mixture to yield **Au_Cl**; full dissolution of the solid will not yield **Au_Cl** upon addition of the reductant. Second, adding solid $CsAuCl_4$ in solvents in which it does not visibly dissolve, with 1,4-diazabicyclo[2.2.2]octane as a reducing agent, yields **Au_Cl** (Supplementary Fig. 2). The polarity of the solvent increases the rate of the solid-to-solid conversion reaction, probably through slight dissolution and reprecipitation. Third, EPR

https://doi.org/10.1038/s41557-023-01305-y

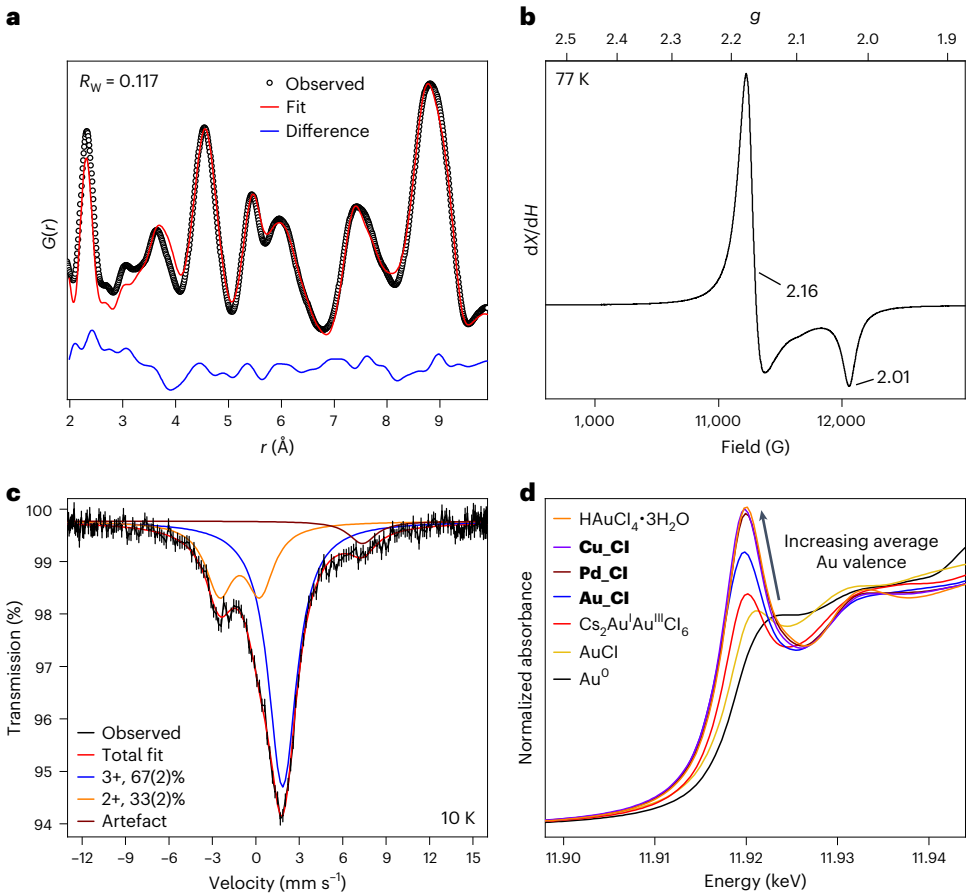

Fig. 3 | Spectroscopic characterization of Au_Cl. a, X-ray PDF analysis showing the experimental and fitted radial distribution function, $G(r)$, and their difference, where R_W is the weighted residual, providing further confirmation of the crystal structure. **b**, Q-band EPR spectrum at 77 K showing an anisotropic signal, consistent with an axially elongated octahedrally coordinated d^9 Au^{2+} centre. The g values shown were extracted from fitting. **c**, ^{197}Au Mössbauer spectrum at 10 K (referenced to a Au^0 foil) showing two doublets corresponding to Au^{3+} and Au^{2+}. The Au^{3+} doublet is visually unresolved due to its small quadrupole splitting. The observed data are plotted as vertical bars representing the measurement uncertainty (1σ). **d**, X-ray absorption near-edge structure spectra collected at the Au L_3 edge showing an increase in the white line intensity with increasing average valence of Au, consistent with the oxidation-state assignment of Au in **Au_Cl**.

measurements of the filtered precursor solution including the reductant give no signal, even when using 5,5-dimethyl-1-pyrroline *N*-oxide as a spin trap[29], indicating that Au^{2+} is not stable in HCl solution and is only stabilized by the solid.

The dark-brown $Cs_4Pd^{II}Au^{III}{}_2Cl_{12}$ (**Pd_Cl**) and yellow-brown $Cs_4Cu^{II}Au^{III}{}_2Cl_{12}$ (**Cu_Cl**) were synthesized as control samples by cooling solutions of CsCl, $AuCl_3$, and $PdCl_2$ or $CuCl_2$ in aqueous HCl from 110 °C to room temperature (Fig. 2; see Methods). Whereas **Pd_Cl** is isostructural with **Au_Cl** (Extended Data Fig. 1), **Cu_Cl** crystallizes in the tetragonal space group $I4_1/amd$ with similarly distorted octahedral coordination of the B-site metals, but with different ordering of the B sites and a halving of the a and b lattice parameter with respect to that of **Au_Cl** (Extended Data Fig. 2)[22,30–34]. Inductively coupled plasma elemental analysis supported the formulas derived from the structural analysis (Supplementary Tables 1 and 2).

As shown by single-crystal XRD and confirmed by powder XRD, **Au_Cl** crystallizes in the tetragonal space group $I4_1cd$ with a structure derived from perovskite by removing one of every four B-site metals in an ordered array to yield quadrupled lattice parameters (Fig. 1b,c, Supplementary Fig. 3 and Supplementary Tables 3–5). X-ray pair distribution function (PDF) analysis, which probes short-range structure, agrees with the average structure provided by XRD (Fig. 3a, Supplementary Fig. 4 and Supplementary Table 6). The $5d^8$ and $5d^9$ valence electronic configurations of Au^{3+} and Au^{2+}, respectively, result in axially elongated octahedral coordination for Au. The one Au^{2+} and two Au^{3+} centres in **Au_Cl** occupy distinct crystallographic sites. In the room-temperature crystal structure, the Au^{3+} and Au^{2+} centres each have nearly equal equatorial Au–Cl bonds, with average lengths (and standard deviations) of 2.290(6) and 2.417(7) Å, respectively (Fig. 1b). These bond lengths are supported by PDF analysis, which shows an increase in the first-shell bond length for **Au_Cl** when compared with **Pd_Cl** or **Cu_Cl**, and by extended X-ray absorption fine-structure (EXAFS) (Fig. 3a, Extended Data Figs. 3 and 4, Supplementary Figs. 5 and 6 and Supplementary Table 7). The Au^{2+} in the molecule Au^{II}(TPP) (tetraphenylporphyrin; TPP^{2-}) features two shorter (2.059(2) Å) and two longer (2.097(2) Å) equatorial bonds, which was attributed to a second-order Jahn–Teller distortion. Such a distortion is not as evident in **Au_Cl**, suggesting that it either is not intrinsic to Au^{2+} or is suppressed in an extended structure with bridging halides.

The ionic radius increases by 0.13 Å when changing from Au^{3+} to Au^{2+} in **Au_Cl**. Similarly, an increase in the average Au–N bond lengths from 2.033(5) to 2.08(3) Å was observed for the molecule Au(TPP)[10], and in ionic solids, the 1.93(5) Å average bond length of square-planar Au^{III}–F elongated to 2.12(5) Å in square-planar Au^{II}–F (refs. 16,17). We do not give an absolute ionic radius for Au^{2+} based on the Shannon radius of Cl^- because the exceptionally high electronegativity of Au (due to

https://doi.org/10.1038/s41557-023-01305-y

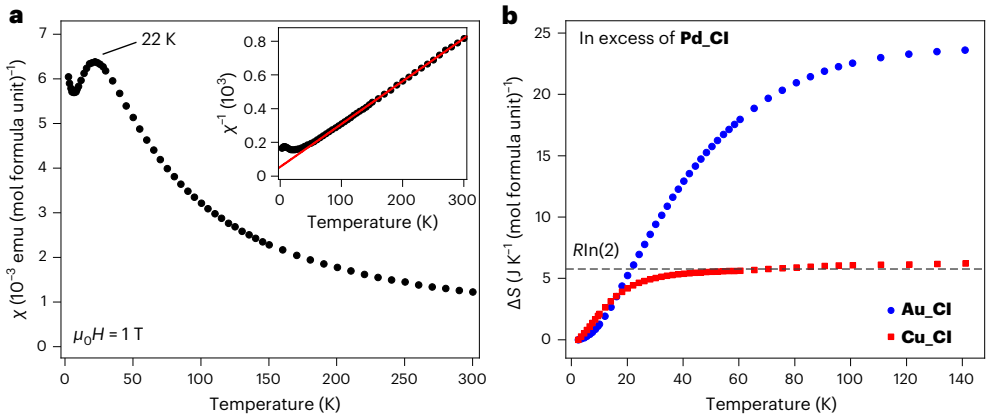

Fig. 4 | Magnetism and heat capacity measurements. a, Temperature-dependent magnetic susceptibility (χ) of **Au_Cl** at an applied field $\mu_0H = 1$ T (diamagnetic correction $\chi_0 = 1.5 \times 10^{-3}$ emu (mol formula unit)$^{-1}$). Inset: Curie–Weiss fit (red line) from 100 K to 300 K. The broad feature at ~22 K corresponds to the onset of short-range antiferromagnetic ordering. **b**, The excess entropy (ΔS) of **Au_Cl** and **Cu_Cl** compared with that of **Pd_Cl**, derived from heat capacity measurements. Dashed line, expected excess entropy for an $S = 1/2$ centre. The greater-than-expected excess entropy of **Au_Cl** may indicate unusual magnetic ordering that requires further study.

relativistic contraction of the 6s orbital, exemplified by its ability to act like a halide[35], as in Cs^+Au^-) results in a high covalency of its bonds, thereby reducing the accuracy of ionic radius estimations. Indeed, such a calculation for Au^{3+} using the well-established square-planar Au–Cl bond length of 2.29 Å and the Shannon radius of Cl^- of 1.81 Å yields an ionic radius for Au^{3+} of 0.48 Å, which is 0.20 Å smaller than the Shannon radius for square-planar Au^{3+} of 0.68 Å.

The long axial bonds of each $AuCl_6$ unit in **Au_Cl** align orthogonally to those of the adjacent $AuCl_6$ units, similar to the recently reported 'gold-cage' perovskites[36]. Along any one unit-cell dimension, three corner-sharing $AuCl_6$ units are grouped together and separated from the adjacent trimer of $AuCl_6$ units by a B-site vacancy. Each such trimer contains two Au^{3+} sites and one Au^{2+} site, oriented with mutually orthogonal long axes. Single-crystal XRD measurements indicated no low-temperature phase transition down to 100 K (Supplementary Table 4). Differential scanning calorimetry measurements indicated a reversible phase transition at ~373 K (Supplementary Fig. 7), which was confirmed by single-crystal XRD measurements at 400 K, revealing a high-temperature structure in the cubic space group $Ia\bar{3}d$ (Supplementary Table 4). This high-temperature structure contains one unique metal site. However, the electronic conductivity does not show a discontinuity at the phase-transition temperature, suggesting that the phase transition has a minimal electronic effect and is probably due to crystallographic disorder between the Au^{2+} and Au^{3+} sites (Supplementary Fig. 8).

Spectroscopic characterization

The unpaired electron in the $d_{x^2-y^2}$ orbital of Au^{2+} and Cu^{2+} is evident in EPR measurements at both 77 K and room temperature. Powders of **Au_Cl** showed an EPR spectrum with $g_\parallel$ and $g_\perp$ values of 2.01 and 2.16, respectively, at 77 K (Fig. 3b and Supplementary Fig. 9). This is inverted with respect to the 77 K EPR spectrum of **Cu_Cl**, which showed $g_\parallel$ and $g_\perp$ values of 2.20 and 2.07, respectively (Extended Data Fig. 5). The inversion of the g tensor between **Cu_Cl** and **Au_Cl** is attributed to the orientation of the $Cu^{II}Cl_6$ and $Au^{II}Cl_6$ units in their respective crystal structures: the long bonds of $Cu^{II}Cl_6$ are all parallel (Extended Data Fig. 2), whereas the long bonds of $Au^{II}Cl_6$ have two orthogonal orientations in a 1:1 ratio (Fig. 1c). A similarly inverted g tensor in two-dimensional (2D) Cu^{II}–Cl perovskites, which also have the long axes of D_{4h} $Cu^{II}Cl_6$ units oriented in two directions in a 1:1 ratio, was ascribed to averaging of the $g_\parallel$ and $g_\perp$ components, which also quenches the hyperfine interactions[37,38]. Thus, the EPR spectrum of **Au_Cl** is a result of individual axial EPR g tensors ($g_\parallel > g_\perp > 2$) averaging in the crystal structure to create an inverted spectrum.

To check if the EPR signal from **Au_Cl** arose from a magnetic impurity, the signal was quantified using **Cu_Cl** as a standard: the integrated signal was 78% of the signal for **Cu_Cl**, consistent with the stoichiometric presence of Au^{2+} within the precision of the technique, which is reduced when comparing two different nuclei (Supplementary Table 8). Additionally, the diamagnetic **Pd_Cl** yielded no discernable EPR signal, further corroborating that the EPR signal did not arise from a common impurity from the synthesis. Further confirmation of the Au oxidation states in **Au_Cl** was provided by ^{197}Au Mössbauer spectroscopy: in addition to a doublet corresponding to Au^{3+}, the spectrum of **Au_Cl** showed a doublet with a lower isomer shift (IS) and quadrupole splitting than the doublet corresponding to Au^{1+} in $Cs_2Au^IAu^{III}Cl_6$, which we assign to Au^{2+}. The spurious feature with an IS of ~7 mm s^{-1} is an instrumental artefact that was present at the same position and same absolute intensity in all scans and was fit as a singlet to account for its contribution. Notably, the integrated intensity ratio of signals from Au^{3+}:Au^{2+} gives a value of 2.0(1), in exact agreement with the expected value, within the error of the measurement (Fig. 3c, Extended Data Fig. 6, Extended Data Table 1 and Supplementary Table 9). While the monotonic decrease of the quadrupole splitting with increasing valence of Au was expected, the IS for Au^{2+} was, surprisingly, lower than that for both Au^{1+} and Au^{3+}, which can be explained by two competing factors: decreasing the valence decreases the IS due to increased nuclear shielding but decreasing the coordination number from four for $Au^{2+/3+}$ to two for Au^{1+} increases the IS for Au^{1+}, consistent with the observed trend for two-, three-, and four-coordinate Au^{1+} complexes[39]. Taken together, this yields a trend for the IS of Au^{2+} (square planar) < Au^{1+} (linear) < Au^{3+} (square planar). X-ray absorption near-edge structure spectra at the L_3 and M_3 edges of Au provided further evidence for Au^{2+} in **Au_Cl**, showing a lower edge energy than samples containing Au in only its 3+ oxidation state, consistent with increased nuclear shielding from a lower average valence of Au (Fig. 3d and Supplementary Figs. 10 and 11). Additionally, the white line intensity, which is a result of transitions of core electrons to empty orbitals in the 5d manifold at the L_3 and M_3 edges of Au, was lower for **Au_Cl**, as expected due to the additional 5d electron in Au^{2+} compared with Au^{3+} (refs. 10,40).

Magnetism

We investigated the magnetism of **Au_Cl** using direct current (DC) magnetization and alternating current (AC) magnetic susceptibility,

https://doi.org/10.1038/s41557-023-01305-y

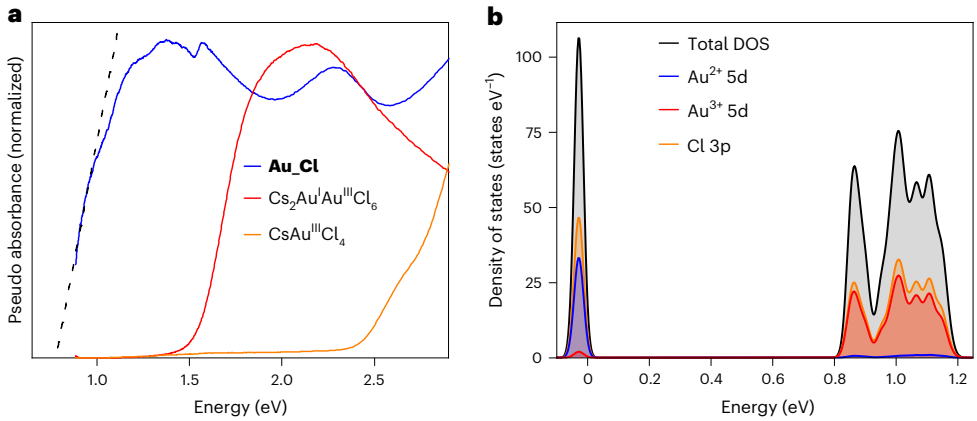

Fig. 5 | Optical and electronic structure characterization. a, UV–vis–NIR absorbance spectra converted from diffuse reflectance spectra using the Kubelka–Munk transformation. The dashed line represents a linear fit to the low-energy absorption of **Au_Cl** to estimate an absorption onset energy of 0.8 eV. **b**, DFT–HSE calculations for **Au_Cl** with antiferromagnetic ordering using coordinates obtained by relaxing the single-crystal XRD structural parameters. The total and the atomic site projected DOS are shown and indicate that the low-energy optical absorption corresponds to intervalence charge transfer between Au^{2+} and Au^{3+}. The valence-band maximum is set at zero energy. We show only the spin-up component; the full DOS plot can be seen in Supplementary Fig. 16.

which revealed a broad peak in the magnetic susceptibility at ~22 K (Fig. 4a and Supplementary Figs. 12–14). The downturn in susceptibility below 22 K indicates antiferromagnetic ordering, with the large breadth of the feature suggesting short-range magnetic order rather than more conventional long-range magnetic order. This is further corroborated by the absence of a sharp feature in the heat capacity measurements (Extended Data Fig. 7). The upturn in susceptibility below ~5 K may be due to minute paramagnetic impurities. Consistent with antiferromagnetic interactions, Curie–Weiss fitting gives a Curie–Weiss temperature, Θ_{CW}, of −21.5(6) K, yielding a coupling constant of $J = 2.47(7)$ meV ($J\,k_B^{-1} = 28.7(8)$ K), assuming three Au^{2+}–Au^{2+} nearest neighbours, as indicated in the single-crystal XRD structure (interatomic distances of 7.39(3), 7.39(3) and 7.59(3) Å). In contrast, **Cu_Cl** behaves as a simple paramagnet down to ~3 K (Extended Data Fig. 8). Quantification of the magnetic moment of **Au_Cl** yields a value for μ_{eff} of 1.77(2) μ_B, as expected for an $S = 1/2$ spin from Au^{2+} ($\mu_{eff} = g\sqrt{S(S+1)} = 1.73\,\mu_B$ for $g = 2$; Supplementary Table 10)[41]. Similar antiferromagnetic ordering has been previously observed in the extended solids $Au^{II}(SbF_6)_2$ (ref. 17) and $Au^{II}_2Au^{III}F_7(SbF_5)_3$ (ref. 16) below 13 K and 50 K, respectively, where the shorter Au^{2+}–Au^{2+} distances (~5.3 Å) compared with those in **Au_Cl** (~7.4 Å) may explain the higher ordering temperature in $Au^{II}_2Au^{III}F_7(SbF_5)_3$.

Heat capacity measurements of **Au_Cl** showed an intriguing amount of excess entropy when compared with diamagnetic **Pd_Cl**, with an approximately four-fold increase with respect to the entropy increase of $R\ln(2)$ expected for $S = 1/2$ spins, where R is the gas constant (Fig. 4b and Extended Data Fig. 7). In contrast, comparison of **Cu_Cl** to **Pd_Cl** showed an excess entropy close to the expected value of $R\ln(2)$. Measurements on larger single crystals of **Au_Cl** formed through slow cooling were similar to those from fine powders precipitated rapidly from solution, suggesting that the increased entropy did not arise from the potentially greater crystallographic disorder in the powders. Our future studies will further investigate the nature of the magnetic ordering and the origin of the greater-than-expected entropy in **Au_Cl**.

Electronic structure

We performed density functional theory (DFT) calculations using the Heyd–Scuseria–Ernzerhof (HSE)[42] hybrid exchange correlation functional as implemented in the Vienna Ab initio Simulation Package (VASP) code[43]. The effects of spin–orbit coupling were assessed with the less accurate but less computationally expensive semi-local functional of Perdew, Burke, and Enzerhof[43,44], where spin–orbit coupling did not meaningfully change the bandgap or magnetic moment (Supplementary Table 11). We therefore neglect spin–orbit coupling to reduce computational complexity in the DFT–HSE calculations presented here. Our calculations were performed using the atomic coordinates obtained from a DFT–HSE structural relaxation starting from the single-crystal XRD structure of **Au_Cl**. Our self-consistent DFT–HSE calculations showed unpaired electron density centred on the putative Au^{2+} sites (0.434 μ_B on average), with some delocalization to its coordinating Cl atoms (consistent with the covalency of the Au–Cl bond), corresponding to an effective total magnetic moment of 0.878 μ_B per Au^{2+}. The calculated magnetic moment on the Au^{2+} confirms the experimental observations and is close to the theoretically expected value of 1 μ_B (gS with $S = 1/2$). Our calculations further predict a ground state consisting of antiferromagnetic ordering of the spins on the Au^{2+} sites, consistent with experiment (Supplementary Fig. 15 and Supplementary Table 12). In contrast, negligible spin polarization was observed in our calculations at the Au^{3+} sites. Our DFT–HSE calculations show an indirect bandgap of 857 meV and a direct bandgap of 859 meV, consistent with the experimental absorption onset value (Fig. 5a). The density of states (DOS) projected onto the Au^{2+} and Au^{3+} 5d orbitals show substantial contributions to the valence and conduction bands, respectively (Fig. 5b and Supplementary Figs. 16 and 17). These calculations suggest that the lowest lying optical transitions are primarily of Au^{2+} to Au^{3+} intervalence charge-transfer character, with some delocalization across the Cl 3p orbitals, consistent with the class II mixed-valence classification by Robin and Day[45].

Optical and electronic properties

The intervalence charge-transfer absorption bands for $Cs_2Au^IAu^{III}X_6$, involving electron transfer between linear Au^IX_2 and square-planar $Au^{III}X_4$, are centred at ~2.0 eV for X = Cl and 1.6 eV for X = Br (ref. 46). The energy required for intervalence charge transfer between Au^{2+} and Au^{3+} is expected to be lower due to the similar square-planar coordination environments of $Au^{II}Cl_4$ and $Au^{III}Cl_4$, which reduces the energy required for atomic rearrangement. Similarly, electronic transport should be more facile in **Au_Cl** compared with $Cs_2Au^IAu^{III}Cl_6$. Indeed, **Au_Cl** has an unusually low absorption onset energy of ~0.8 eV, probably due to the low-energy intervalence charge-transfer absorption that peaks at ~1.3 eV (Extended Data Fig. 9). The room-temperature electronic conductivity of **Au_Cl** is $2.58(1) \times 10^{-6}$ S cm^{-1}, nearly three orders of magnitude higher than the conductivity of $Cs_2Au^IAu^{III}Cl_6$ and two orders of magnitude higher than the conductivity of $Cs_2Au^IAu^{III}Br_6$, measured similarly (Supplementary Fig. 18 and Supplementary Table 13).

Stability

Although Au^{2+} easily disproportionates to Au^{3+} and Au^{1+}(refs. 3,12,47), it appears to be stabilized in **Au_Cl**, with no noticeable decomposition over months of storage in ambient conditions. Repeated EPR measurements taken on the same **Au_Cl** powder sample exposed to ambient atmosphere showed no change after a 2 day exposure and slight reduction of the signal intensity after a 10 day exposure or after heating the powder in air at 150 °C for 24 h (Supplementary Fig. 19). Furthermore, unlike organic–inorganic perovskites that begin to lose volatile organic molecules well below 100 °C (ref. 48), thermogravimetric analysis of the all-inorganic **Au_Cl** at a rate of 1 °C min^{-1} indicated no mass loss until ~250 °C (Supplementary Fig. 20 and Supplementary Table 14), while heating **Au_Cl** at 150 °C in ambient atmosphere for 24 h showed no discernable decomposition by powder XRD (Supplementary Fig. 21).

Conclusions

The redox non-innocence of the ligand has been implicated in stabilizing mononuclear Au^{2+} in molecules[6]. For example, nuclear spin coupling constants extracted from experimental EPR spectra of these molecules indicate that ~15% of the spin density resides at the Au (refs. 49,50). In contrast, chlorides are simple donor ligands, not known to exhibit variable oxidation states when coordinated to metals. Almost all metal chlorides have highly ionic bonds because Cl is very electronegative. However, the high electronegativity[35] of Au imparts a large degree of covalency to the Au–Cl framework, which may be the origin of the unusual stability of **Au_Cl**. Our experiments are supported by DFT calculations that predict charge disproportionation leading to distinct Au^{2+} and Au^{3+} sites and coordination environments, opening up a bandgap and resulting in an uncompensated spin moment centred at the Au^{2+} sites, in agreement with measurements. The ease of synthesis and stability of **Au_Cl** enables the further study of the chemistry of Au^{2+}. Further, the spectroscopic signatures of Au^{2+} bound to simple ligands reported here allow for the identification of transient Au^{2+} species in catalytic cycles[3]. By realizing uncommon oxidation states within the halide perovskite framework, we may also set the stage for accessing electronic states associated with exotic transport phenomena more commonly seen in the oxide perovskites. Indeed, Au^{2+} and Au^{3+} are isoelectronic with the cuprate superconductors comprising Cu^{2+} and Cu^{3+}, and the doping and transport properties of $Au^{2+/3+}$ perovskites warrant further study.

Online content

Any methods, additional references, Nature Portfolio reporting summaries, source data, extended data, supplementary information, acknowledgements, peer review information; details of author contributions and competing interests; and statements of data and code availability are available at https://doi.org/10.1038/s41557-023-01305-y.

References

1. Norrby, L. J. Why is mercury liquid? Or, why do relativistic effects not get into chemistry textbooks? *J. Chem. Educ.* **68**, 110 (1991).
2. Hopkinson, M. N., Tlahuext-Aca, A. & Glorius, F. Merging visible light photoredox and gold catalysis. *Acc. Chem. Res.* **49**, 2261–2272 (2016).
3. Heinze, K. The quest for mononuclear gold(II) and its potential role in photocatalysis and drug action. *Angew. Chem. Int. Ed. Engl.* **56**, 16126–16134 (2017).
4. Waters, J. H. & Gray, H. B. A stable paramagnetic complex of gold. *J. Am. Chem. Soc.* **87**, 3534–3535 (1965).
5. Ihlo, L., Böttcher, R., Olk, R. M. & Kirmse, R. A single-crystal electron paramagnetic resonance, ^{13}C and ^{1}H electron nuclear double resonance study of tetra-*n*-butylammonium-bis (1,2-dicyanoethylene-1,2-dithiolato)aurate(II), $[(n\text{-}C_4H_9)_4N]_2[Au^{II}(mnt)_2]$. *Inorganica Chim. Acta* **281**, 160–164 (1998).
6. Shaw, J. L. et al. Redox non-innocence of thioether macrocycles: elucidation of the electronic structures of mononuclear complexes of gold(II) and silver(II). *J. Am. Chem. Soc.* **128**, 13827–13839 (2006).
7. Kampf, M., Griebel, J. & Kirmse, R. EPR-spektroskopische Charakterisierung (X-, Q-Band) monomerer Ag^{II}- und Au^{II}-Komplexe der Thiakronenether [12]anS_4, [16]anS_4, [18]anS_6 und [27]anS_9. *Z. Anorg. Allg. Chem.* **630**, 2669–2676 (2004).
8. Huang, D. et al. Crystallographic, electrochemical, and electronic structure studies of the mononuclear complexes of Au(I)/(II)/(III) with [9]$aneS_2O$ ([9]$aneS_2O$ = 1-oxa-4,7-dithiacyclononane). *Inorg. Chem.* **47**, 9919–9929 (2008).
9. Blake, A. J. et al. Bis(1,4,7-trithiacyclononane)gold dication: a paramagnetic, mononuclear Au^{II} complex. *Angew. Chem. Int. Ed.* **29**, 197–198 (1990).
10. Preiß, S. et al. Structure and reactivity of a mononuclear gold(II) complex. *Nat. Chem.* **9**, 1249–1255 (2017).
11. Schmidbaur, H., Mandl, J. R., Frank, A. & Huttner, G. Synthese und Kristallstruktur eines zweikernigen Ylid-Komplexes mit Metall-Metall-Bindung zwischen Goldatomen der Oxidationsstufe +II. *Chem. Ber.* **109**, 466–472 (1976).
12. Gimeno, M. C. in *Modern Supramolecular Gold Chemistry* Ch. 1 (ed. Laguna, A.) 1–63 (Wiley, 2008).
13. Wickleder, M. S. $AuSO_4$: a true gold(II) sulfate with an Au_2^{4+} ion. *Z. Anorg. Allg. Chem.* **627**, 2112–2114 (2001).
14. Liu, X. J., Moritomo, Y., Nakamura, A. & Kojima, N. Pressure-induced phase transition in mixed-valence gold complexes $Cs_2Au_2X_6$ (*X* = Cl and Br). *J. Chem. Phys.* **110**, 9174–9178 (1999).
15. Kojima, N. et al. P–T phase diagram and gold valence state of the perovskite-type mixed-valence compounds $Cs_2Au_2X_6$ (X = Cl, Br, and I) under high pressures. *J. Am. Chem. Soc.* **116**, 11368–11374 (1994).
16. Hwang, I.-C. & Seppelt, K. The reduction of AuF_3 in super acidic solution. *Z. Anorg. Allg. Chem.* **628**, 765–769 (2002).
17. Elder, S. H., Lucier, G. M., Hollander, F. J. & Bartlett, N. Synthesis of Au(II) fluoro complexes and their structural and magnetic properties. *J. Am. Chem. Soc.* **119**, 1020–1026 (1997).
18. Seidel, S. & Seppelt, K. Xenon as a complex ligand: the tetra xenono gold(II) cation in $AuXe_4^{2+}(Sb_2F_{11}^-)_2$. *Science* **290**, 117–118 (2000).
19. Drews, T., Seidel, S. & Seppelt, K. Gold–xenon complexes. *Angew. Chem. Int. Ed.* **41**, 454–456 (2002).
20. Odenthal, R. H. & Hoppe, R. Fluorargentate(II) der Alkalimetalle. *Monatsh. Chem.* **102**, 1340–1350 (1971).
21. Okazaki, A. & Suemune, Y. The crystal structure of $KCuF_3$. *J. Phys. Soc. Jpn.* **16**, 176–183 (1961).
22. Wells, H. L. Some complex chlorides containing gold. II. Cesium triple salts. *Am. J. Sci.* **3**, 315–326 (1922).
23. Wolf, N. R., Connor, B. A., Slavney, A. H. & Karunadasa, H. I. Doubling the stakes: the promise of halide double perovskites. *Angew. Chem. Int. Ed. Engl.* **60**, 16264–16278 (2021).
24. Elliott, N. & Pauling, L. The crystal structure of cesium aurous auric chloride, $Cs_2AuAuCl_6$, and cesium argentous auric chloride, $Cs_2AgAuCl_6$. *J. Am. Chem. Soc.* **60**, 1846–1851 (1938).
25. Eijndhoven, J. C. M. T.-v & Verschoor, G. C. Redetermination of the crystal structure of $Cs_2AuAuCl_6$. *Mat. Res. Bull.* **9**, 1667–1670 (1974).
26. Kitagawa, H., Kojima, N., Matsushita, N., Ban, T. & Tsujikawa, I. Studies of mixed-valence states in three-dimensional halogen-bridged gold compounds, Cs_2AuAuX_6 (X = Cl, Br or I). Part 1. Synthesis, X-ray powder diffraction, and electron spin resonance studies of $CsAu_{0.6}Br_{2.6}$. *J. Chem. Soc. Dalton Trans.* **11**, 3115–3119 (1991).

27. Kitagawa, H., Kojima, N. & Nakajima, T. Studies of mixed-valence states in three-dimensional halogen-bridged gold compounds, Cs_2AuAuX_6 (X = Cl, Br or I). Part 2. X-ray photoelectron spectroscopic study. *J. Chem. Soc. Dalton Trans.* **11**, 3121–3125 (1991).
28. Kitagawa, H., Kojima, N. & Sakai, H. Studies of mixed-valence states in three-dimensional halogen-bridged gold compounds, Cs_2AuAuX_6 (X = Cl, Br or I). Part 3. Gold-197 Mössbauer spectroscopic study. *J. Chem. Soc. Dalton Trans.* **12**, 3211–3215 (1991).
29. Bilski, P., Reszka, K., Bilska, M. & Chignell, C. F. Oxidation of the spin trap 5,5-dimethyl-1-pyrroline *N*-oxide by singlet oxygen in aqueous solution. *J. Am. Chem. Soc.* **118**, 1330–1338 (1996).
30. Linus Pauling Day-by-Day (September 6, 1937). *Oregon State Univ.* http://scarc.library.oregonstate.edu/ (1937).
31. Ferrari, A., Cecconi, R. & Cavalca, L. Isomorfismo fra esacloroaurati di elementi a valenz diversa.—Nota IV sull'sistenza degli esacloroaurati. *Gazz. Chim. Ital.* **73**, 23–29 (1943).
32. Ferrari, A., Cavalca, L. & Nardelli, M. Su alcuni cloroaurati e su un caso di ampio isomorfismo di massa. *Gazz. Chim. Ital.* **85**, 137–144 (1955).
33. Gomm, P. S. & Underhill, A. E. Electrical conduction studies on the mixed-valence triple salts of gold. *Inorg. Chem. Nucl. Chem. Lett.* **10**, 309–313 (1974).
34. Heines, P. *Darstellung und Untersuchungen ternärer und quaternärer Halogenopalladate mit besonderer Beachtung von Redoxreaktionen: Pd(II)/Pd(IV) im Festkörper*. Thesis, Univ. Dortmund (2004).
35. Jansen, M. The chemistry of gold as an anion. *Chem. Soc. Rev.* **37**, 1826–1835 (2008).
36. Lindquist, K. P., Boles, M. A., Mack, S. A., Neaton, J. B. & Karunadasa, H. I. Gold-cage perovskites: a three-dimensional $Au^{II}I$–X framework encasing isolated MX_6^{3-} octahedra (M^{III} = In, Sb, Bi; X = Cl^-, Br^-, I^-). *J. Am. Chem. Soc.* **143**, 7440–7448 (2021).
37. Soos, Z. G., McGregor, K. T., Cheung, T. T. P. & Silverstein, A. J. Antisymmetric and anisotropic exchange in ferromagnetic copper(II) layers. *Phys. Rev. B* **16**, 3036–3048 (1977).
38. Connor, B. A. et al. Alloying a single and a double perovskite: a $Cu^{+/2+}$ mixed-valence layered halide perovskite with strong optical absorption. *Chem. Sci.* **12**, 8689–8697 (2021).
39. Parish, R. V. in *Mössbauer Spectroscopy Applied to Inorganic Chemistry* (ed. Long, G. J.) 577–617 (Springer, 1984).
40. Tanino, H. & Takahashi, K. Valence study of Au in $Cs_2Au(I)Au(III)Cl_6$ and $Cs_2Ag(I)Au(III)X_6$ (X = Cl, Br) by X-ray absorption spectra at the Au L_3 edge. *Solid State Commun.* **59**, 825–827 (1986).
41. Eisberg, R. & Resnick, R., *Quantum Physics of Atoms, Molecules, Solids, Nuclei, and Particles* (John Wiley & Sons, 1985).
42. Heyd, J., Scuseria, G. E. & Ernzerhof, M. Hybrid functionals based on a screened Coulomb potential. *J. Chem. Phys.* **118**, 8207–8215 (2003).
43. Kresse, G. & Furthmüller, J. Efficient iterative schemes for *ab initio* total-energy calculations using a plane-wave basis set. *Phys. Rev. B* **54**, 11169–11186 (1996).
44. Perdew, J. P., Burke, K. & Ernzerhof, M. Generalized gradient approximation made simple. *Phys. Rev. Lett.* **77**, 3865–3868 (1996).
45. Robin, M. B. & Day, P. in *Advances in Inorganic Chemistry and Radiochemistry* Vol. 10 (eds Emeléus, H. J. & Sharpe, A. G.) 247–422 (Academic Press, 1968).
46. Kojima, N. & Kitagawa, H. Optical investigation of the intervalence charge-transfer interactions in the three-dimensional gold mixed-valence compounds $Cs_2Au_2X_6$ (X = Cl, Br or I). *J. Chem. Soc. Dalton Trans.* **3**, 327–331 (1994).
47. Bergendahl, T. J. The oxidation states of gold. *J. Chem. Educ.* **52**, 731–732 (1975).
48. Slavney, A. H. et al. Chemical approaches to addressing the instability and toxicity of lead–halide perovskite absorbers. *Inorg. Chem.* **56**, 46–55 (2017).
49. Herring, F. G. et al. Generation of gold ions in the solid state or in fluorosulfuric acid solution and their identification by ESR. *J. Am. Chem. Soc.* **114**, 1271–1277 (1992).
50. Schlupp, R. L. & Maki, A. H. Paramagnetic resonance investigation of bis(maleonitriledithiolato)gold(II) a formal gold(II) complex. *Inorg. Chem.* **13**, 44–51 (1974).

Methods

General methods

All manipulations were performed in ambient atmosphere and at room temperature unless otherwise noted. All chemicals, of reagent grade or higher purity, were purchased from commercial vendors and used as received, unless otherwise noted.

Synthesis of $Cs_4Au^{II}Au^{III}{}_2Cl_{12}$ (Au_Cl)

Solid $Cs_4Au^{II}Au^{III}{}_2Cl_{12}$ (**Au_Cl**) was synthesized by partial reduction of Au^{3+} to Au^{2+} in 6 M HCl. The affinity of the Au^{3+} source, $HAuCl_4{\cdot}3H_2O$, for atmospheric moisture complicated weighing small amounts of this material. Therefore, all syntheses with $HAuCl_4{\cdot}3H_2O$ used stock solutions. Solid $HAuCl_4{\cdot}3H_2O$ was handled with a glass pipet to avoid galvanic exchange between Au^{3+} and the steel spatula blade. Stock solutions of the precursors for **Au_Cl**: 1 M CsCl from 168 mg (1.00 mmol) of CsCl in 1 ml of 6 M HCl, 0.5 M $AuCl_3$ from 197 mg (0.500 mmol) of $HAuCl_4{\cdot}3H_2O$ in 1 ml of 6 M HCl, and 0.1 M ascorbic acid from 35.2 mg (0.200 mmol) of L-ascorbic acid in 2 ml of 6 M HCl. The ascorbic acid stock solutions were freshly prepared on the day of the synthesis. In a typical synthesis of **Au_Cl** powder, 375 µl of CsCl and 250 µl of $AuCl_3$ stock solutions were combined in a 4 ml vial. A yellow precipitate formed immediately, identified as $CsAuCl_4$ (ref. 51). Then, 208 µl of the ascorbic acid solution was added, the solution was sonicated in an ultrasonic water bath for 5 min with periodic manual agitation to ensure complete mixing, and allowed to rest for 10 min. The reaction temperature was kept at <30 °C; even mild heating caused over-reduction to Au^{1+}, producing $Cs_2Au^{I}Au^{III}Cl_6$ (ref. 24). The dark-green solid was isolated from the mother liquor by filtration and dried under reduced pressure. A typical yield was 63% (~40 mg). Scaling up this synthesis required repetition of this procedure in separate 4 ml vials; attempts at directly scaling up in one reaction vessel often yielded $Cs_2Au^{I}Au^{III}Cl_6$ and $CsAuCl_4$ in addition to **Au_Cl**. Because the synthesis appears to proceed via a solid intermediate ($CsAuCl_4$), we suspect that the local concentrations and surface area of the solids play an important role in the synthesis of **Au_Cl**; that is, in a large batch, the lower surface area-to-volume ratio of the solid may lead to over-reduction of the Au^{3+} to Au^{1+} and formation of the $Cs_2Au^{I}Au^{III}Cl_6$ side product. Other mild reducing agents besides ascorbic acid, such as hydrazine, could be used to form **Au_Cl**. Furthermore, $CsAuCl_4$ could be partially reduced to form **Au_Cl** by placing solid $CsAuCl_4$ powder into a weak or non-solvent, such as acetonitrile, benzene or hexanes with a stoichiometric amount of 1,4-diazabicyclo[2.2.2]octane (assuming it is a two-electron reductant[52]) and sonicating for 5 min or allowing it to sit for 48 h (Supplementary Fig. 2).

Single crystals of **Au_Cl** were formed through adventitious reduction of Au^{3+} in 6 M aqueous HCl at elevated temperature. In a typical crystallization, 125 µl of CsCl and 83 µl of $AuCl_3$ solutions and 300 µl of 6 M HCl were combined in a 4 ml vial. The solution was heated at 110 °C for 1 h and then cooled to room temperature at a rate of 1 °C h^{-1}. The primary product of this crystallization was $CsAuCl_4$, with crystals of **Au_Cl** forming as a side product (<1 mg). Fragments of the **Au_Cl** crystals were used for single-crystal XRD. Additional side products identified were $Cs_2Au^{I}Au^{III}Cl_6$, $Cs_5Au_3Cl_{14}$ (ref. 53) and Au^0. Each product was distinguished by its colour and appearance under the microscope: $CsAuCl_4$ is yellow (needles), $Cs_5Au_3Cl_{14}$ is red, Au^0 is golden and strongly reflective and $Cs_2Au^{I}Au^{III}Cl_6$ appears black with bottom lighting but has a strong golden specular reflectance when viewed with direct overhead lighting, whereas **Au_Cl** forms black crystals with a cubic or rectangular prismatic habit that do not exhibit golden specular reflectance when viewed with direct overhead lighting. Crystals of **Au_Cl** were manually separated from the product mixture in Paratone-N immersion oil using direct overhead lighting with a microscope and a needle, after which the Paratone-N oil was removed with copious hexanes.

Single crystals of **Au_Cl** were also formed through adventitious reduction of Au^{3+} by Cl^- in 70% (v/v) ethanol in ambient conditions. Stock solutions of the precursors for **Au_Cl**: 1 M CsCl from 168 mg (1.00 mmol) of CsCl in 1 ml of 70% ethanol and 0.5 M $AuCl_3$ from 197 mg (0.500 mmol) of $HAuCl_4{\cdot}3H_2O$ in 1 ml of 70% ethanol. In a typical crystallization, 125 µl of CsCl and 83 µl of $AuCl_3$ solutions and 500 µl of 70% ethanol were combined in a 2 ml scintillation vial with a septum cap. Mild sonication or manual agitation of the precursor solution resulted in the formation of a small amount of dark-green powder. A 40 mm 21 gauge needle inserted into the septum cap was used to vent the vial. The vial was left in the dark to slowly evaporate for 10 days, after which single crystals of **Au_Cl** were isolated via vacuum filtration and washed with ~10 ml of 0 °C anhydrous ethanol (>99.5%). After 10 days, pure **Au_Cl** was isolated with a typical yield of 13% (~5 mg). While further evaporation of the solvent may result in higher yields, complete evaporation results in the formation of $CsAuCl_4$ as a side product. Scaling up by a factor of five in a 5 ml scintillation vial yielded pure **Au_Cl**. Doubling the reactant concentration resulted in the formation of only $Cs_5Au_3Cl_{14}$. The ethanol-based synthesis was used only for the study testing the presence of Cl_2 in the crystallization solution; all other measurements were carried out on **Au_Cl** synthesized in HCl.

Synthesis of $Cs_4CuAu_2Cl_{12}$ (Cu_Cl) and $Cs_4PdAu_2Cl_{12}$ (Pd_Cl)

The solids **Pd_Cl** and **Cu_Cl** were prepared using a modified reported procedure[34]. Here, the metal–chloride salts were dissolved in hot 6 M HCl and cooled to room temperature. Stock solutions of the precursors: 0.5 M $CuCl_2$ from 67.2 mg (0.500 mmol) of $CuCl_2$ in 1 ml of 6 M HCl and 0.5 M $PdCl_2$ from 88.7 mg (0.500 mmol) of $PdCl_2$ in 1 ml of 6 M HCl. In a typical synthesis of **Cu_Cl**, 200 µl of CsCl, 40 µl of $AuCl_3$ and 200 µl of $CuCl_2$ stock solutions and 1.6 ml of 6 M HCl were combined in a 4 ml vial. After heating at 110 °C for 1 h to dissolve the brown precipitate, the solution was cooled to room temperature at a rate of 1 °C h^{-1}. The black/dark-brown crystals were isolated from the mother liquor by filtration and dried under reduced pressure. Similarly, the black solid **Pd_Cl** was synthesized using 100 µl of CsCl, 100 µl of $AuCl_3$ and 100 µl of $PdCl_2$ solution and 2.85 ml of 6 M HCl.

Synthesis of $CsAuCl_4$

The known solid $CsAuCl_4$(refs. 51,54) was synthesized using a modified reported procedure. In a typical synthesis, 125 µl of CsCl and 83 µl of $AuCl_3$ stock solutions and 250 µl of 6 M HCl were combined in a 4 ml vial. The reaction mixture was heated at 110 °C for 5 min to dissolve the yellow precipitate and the solution was then allowed to cool to room temperature for 2 h. The yellow crystals were isolated from the mother liquor by filtration and dried under reduced pressure. Prolonged heating or a very slow cooling rate (hours to days) of the solution produced the side products **Au_Cl**, $Cs_2Au^{I}Au^{III}Cl_6$ and Au^0.

Synthesis of $Cs_2Au^{I}Au^{III}Cl_6$ and $Cs_2Au^{I}Au^{III}Br_6$

The known double perovskites $Cs_2Au^{I}Au^{III}Cl_6$ and $Cs_2Au^{I}Au^{III}Br_6$ have been previously synthesized out of aqueous HX solution and via solid-state methods[22,55]. Here, we synthesized them by partial reduction of Au^{3+} with ascorbic acid in hot aqueous HX solution. In a typical synthesis, 125 µl of CsCl and 83 µl of $AuCl_3$ stock solutions and 250 µl of 6 M HCl were combined in a 4 ml vial. A yellow precipitate formed immediately. Then, 208 µl of ascorbic acid solution was added to the reaction mixture, which was heated at 50 °C for 30 min with periodic manual agitation and then allowed to cool for 2 h. The black precipitate was isolated from the mother liquor by filtration and dried under reduced pressure. Scaling up this synthesis required repetition of the synthesis in separate 4 ml vials; attempts at directly scaling up in one reaction vessel yielded the side products Au^0 and **Au_Cl** in addition to the main product, $Cs_2Au^{I}Au^{III}Cl_6$.

Stock solutions of the precursors for $Cs_2Au^{I}Au^{III}Br_6$: 1 M CsBr from 213 mg (1.00 mmol) of CsBr in 1 ml of 9 M HBr and 0.5 M $AuBr_3$ from 197 mg (0.500 mmol) of $HAuCl_4 \cdot 3H_2O$ in 1 ml of 9 M HBr. A typical synthesis involved adding 125 µl of CsBr and 83 µl of $AuBr_3$ stock solutions

and 500 µl of 9 M HBr to a 4 ml vial. A black precipitate formed immediately. Then, 100 µl of the ascorbic acid solution was added, and the reaction mixture was heated at 110 °C for 30 min with periodic manual agitation, after which the solution was allowed to cool for 2 h. The black precipitate was isolated from the mother liquor by filtration and dried under reduced pressure. This reaction could be directly scaled up.

Elemental analysis

The abundance of Cs, Au and Cu in **Au_Cl**, **Pd_Cl** and **Cu_Cl** was determined using a Thermo Scientific XSERIES 2 inductively coupled plasma mass spectrometer, while the abundance of Pd in **Pd_Cl** was determined using a Thermo Scientific ICAP 6300 Duo View inductively coupled plasma optical emission spectrometer. Inductively coupled plasma analysis was conducted in dilute aqua regia (3:1 HCl and HNO_3, diluted to 1.8% (v/v) acid in H_2O) to stabilize Au in solution. Elemental abundances reported in Supplementary Tables 1 and 2 represent the averages across three measurements of each sample.

Crystal structure determination

Crystals of **Au_Cl**, **Pd_Cl**, and **Cu_Cl** were coated with Paratone-N oil, mounted on a Kapton loop and transferred to a Bruker D8 diffractometer equipped with a Photon II CMOS detector. Frames were collected using ω and ψ scans with 17.012 keV synchrotron radiation (λ = 0.72880 Å) at beamline 12.2.1 at the Advanced Light Source at Lawrence Berkeley National Laboratory or with 17.445 keV Mo-Kα radiation (λ = 0.71073 Å) at the Stanford Nano Shared Facilities. An Oxford Cryostream was used where crystals were measured at temperatures other than room temperature.

Optical spectroscopy

Solid-state ultraviolet–visible–near-infrared (UV–vis–NIR) diffuse reflectance spectra were collected using a Shimadzu UV2600 spectrophotometer equipped with an integrating sphere in reflectance mode. Powders or crystals were pulverized and diluted in a mull with $BaSO_4$ by a factor of ~20, by mass, and pressed into a sample puck, which was mounted at the rear of the integrating sphere. A sample puck filled with pure $BaSO_4$ was used as a blank.

Spectroscopic studies to detect the presence of Cl_2 used the same spectrophotometer that was instead equipped for transmission measurements in a quartz cuvette. Control samples were prepared of the crystallization solution of **Au_Cl** in 70% (v/v) ethanol, which had been evaporated for 10 days (in 'Synthesis of $Cs_4Au^{II}Au^{III}{}_2Cl_{12}$'), and of 0.5 M NaI, 1.0 M CsCl and 0.5 M $HAuCl_4$ solutions in 70% ethanol. For optical measurements, 50 µl of 0.5 M $HAuCl_4$ was diluted with 2.95 ml of 70% ethanol. Solutions of 0.5 M NaI and 1.0 M CsCl were measured without dilution. A 0.7 mM NaI_3 control solution was prepared by adding 0.5 mg I_2 to 3 ml of the 0.5 M NaI solution. The test sample was prepared by adding 2 µl each of the crystallization solution of **Au_Cl** and the 0.5 M NaI solution to 3.00 ml of 70% ethanol. The same cuvette filled with 70% ethanol was used as a blank.

^{197}Au Mössbauer spectroscopy

^{197}Au Mössbauer spectra were obtained for **Au_Cl** and $Cs_2Au^{I}Au^{III}Cl_6$. The 19.89 h ^{197}Pt used as the source for ^{197}Au Mössbauer spectroscopy was created by neutron activation of a 100 mg piece of enriched ^{196}Pt in the McMaster Nuclear Reactor, located on the campus of McMaster University in Hamilton, Ontario. The initial activity of the source as delivered at the start of the measurements was ~200 MBq (5.4 mCi). The 77.35 keV γ rays from the source were detected using a high-purity Ge detector with careful pulse-height windowing used to minimize contamination from the strong 77.98 keV Au-Kβ emission from the source. The sample and source were mounted vertically in a He-flow cryostat so that both could be cooled to 10 K for the measurements. The source was driven in sinusoidal mode with the motion calibrated using a standard ^{57}Co(Rh)/α-Fe foil. All isomer shifts are quoted relative to a metallic Au foil standard that was run immediately before starting the measurements on the samples.

EPR spectroscopy and spin quantification

X-band EPR spectra were obtained with a Bruker EMX spectrometer, an ER 041 XG microwave bridge and an ER4119HS resonator. Powders or crystals were pulverized and diluted into a mull with 0.6 g KCl to a concentration of approximately 5% (w/w) to avoid signal saturation. The samples of **Au_Cl** measured over a period of 10 days at room temperature or 24 h at 150 °C to check for degradation (Supplementary Fig. 19) were not diluted; signal saturation did not occur. The samples were loaded into quartz EPR tubes (Wilmad-LabGlass; 4 mm outer diameter) and packed with a consistent number of bounces. A sample temperature of 77 K was maintained using a liquid nitrogen finger Dewar. Collections at room temperature were obtained by directly placing the sample in the resonator. X-band EPR parameters: frequency ~9.9 GHz (room temperature) or 9.4 GHz (77 K), power ~1 mW, receiver gain 10 dB, modulation frequency 100 kHz, modulation amplitude 4.00 G, time constant 0.01 ms and conversion time 4 ms. Power sweeps were performed to verify samples were in non-saturating conditions. Ten to twenty scans were averaged for each sample. To check whether anything in the solids other than Cu^{2+} or Au^{2+} was responsible for the EPR signals, **Pd_Cl** was measured as a control; it produced no measurable EPR signal.

The Q-band EPR spectra of **Au_Cl** were obtained with a Bruker EMX spectrometer, an ER051QT microwave bridge and an ER 5106QT resonator. A powder sample of **Au_Cl** was loaded into a quartz EPR tube (Wilmad-LabGlass; 1.6 mm outer diameter) that was inserted into the resonator using a sample rod. The spectrum was collected at 77 K by flowing liquid helium through an Oxford continuous flow CF935 cryostat. The spectrum at room temperature was collected in the same setup but without introducing cryogens. Q-band EPR parameters: frequency ~34.0 GHz, power ~0.2 mW (room temperature) or 1.0 mW (77 K), receiver gain 29 dB (room temperature) or 15 dB (77 K), modulation frequency 100 kHz, modulation amplitude 5.00 G, time constant 0.01 ms and conversion time 6 ms.

Total X-ray scattering and PDF analysis

Total X-ray scattering experiments were carried out at beamline 11-ID-B at the Advanced Photon Source at Argonne National Laboratory. Powder samples were ground using a mortar and pestle before being packed into Kapton capillaries with 1.1 mm outer diameters. The samples were measured at room temperature using 86.58 keV (λ = 0.1432 Å) or 58.62 keV (λ = 0.2115 Å) synchrotron radiation, a spot size of 100 µm × 100 µm, an exposure time of 0.1–0.5 s, and repeated exposures for a total collection time of 5 min. The sample-to-detector distance was 25 cm for collections using 86.58 keV (λ = 0.1432 Å) radiation and 18 cm for collections using 58.62 keV (λ = 0.2115 Å) radiation and was calibrated using a sample of CeO_2. A scan of an empty Kapton capillary was collected for background subtraction.

XAS

X-ray absorption spectroscopy (XAS) data were collected at beamlines 4-1 (Au L_3 edge, Cu K edge and Pd K edge) and 4-3 (Au M_3 edge) at the Stanford Synchrotron Radiation Lightsource at SLAC National Accelerator Laboratory following a previously described method[36]. Data were collected at the Au L_3 edge of $HAuCl_4{\cdot}3H_2O$, AuCl, $Cs_2Au^{I}Au^{III}Cl_6$, **Au_Cl**, **Pd_Cl** and **Cu_Cl** and at the Au M_3 edge on the same compositions, except for $HAuCl_4{\cdot}3H_2O$. Data were collected at the Pd K edge of **Pd_Cl** and at the Cu K edge of **Cu_Cl**. For Au L_3-edge, Pd K-edge and Cu K-edge collections, samples were diluted in a mull with hexagonal boron nitride such that the total absorption of the sample, once ground using a mortar and pestle and pressed into pellets with thicknesses of ~1 mm, would approximately equal *e*. The sample mulls were pressed into pellets under ~3,000 kg of pressure to ensure uniform density.

Transmission and fluorescence data were collected for all samples, with simultaneous transmission spectra collected on a Au, Pd or Cu foil in every scan for reference. The fluorescence data appeared to show self-absorption effects for the Au L_3-edge and Pd K-edge data; therefore, transmission data were used for all Au L_3-edge and Pd K-edge analysis. Upon comparison to the transmission data, the fluorescence data at the Cu K edge showed no obvious self-absorption effects and provided superior signal-to-noise ratios to the transmission data; therefore, fluorescence data were used for all Cu K-edge analyses. For Au M_3-edge collections, samples were ground using a mortar and pestle and subsequently spread into a uniform layer on Saint-Gobain CHR M60 low-sulfur tape. Transmission and fluorescence data were collected for all samples. The transmission and fluorescence data were qualitatively identical, but the fluorescence data provided superior signal-to-noise ratios to the transmission data; therefore, fluorescence data were used for all Au M_3-edge analysis. A fluorescence spectrum was collected on a Au foil for reference before collecting on the samples.

Electronic conductivity measurements

Electrochemical impedance spectroscopy measurements were carried out on pressed powders of **Au_Cl**, $Cs_2Au^{I}Au^{III}Cl_6$ and $Cs_2Au^{I}Au^{III}Br_6$ using a four-point probe van der Pauw configuration in a custom-built setup with a Bio-Logic VSP300 Potentiostat/Galvanostat. Powders were pressed into circular pellets with ~0.7 mm thicknesses and 13 mm diameters at 4,500 kg of pressure for 30 s inside a nitrogen-filled glovebox. Pellets were cut into squares with side lengths of ~5 mm. The custom-built sample mount consisted of a copper-metal base insulated from four stainless-steel metal fingers that were used to establish electrical contact to the sample. A thermistor was fastened to the copper base near the sample to measure sample temperature. The pellet samples were mounted on a sapphire substrate to insulate the sample from the copper base but allow for thermal equilibration. To decrease contact resistance and prevent chemical reaction between the sample and the metal fingers, four graphitic carbon pads were hand painted along the perimeter of the sample pellet. The surface area of the carbon pads was <1 mm^2 and the contact-to-contact distance was ~5 mm. Carbon pads were painted from a graphite/toluene suspension that was prepared from the commercially available PELCO colloidal graphite (Ted Pella). As isopropanol may cause slight degradation of the surface of the pellet, it was removed under vacuum and a new slurry was made with dry toluene to a concentration of 100 mg ml^{-1}. This mixture is less colloidally stable than the original isopropanol version, and therefore was sonicated immediately before use to resuspend any precipitated solids. The sample mount was contained within a sealed, opaque and electrically grounded metal box with a very low flow of nitrogen (~1 bubble s^{-1} with an oil-filled bubbler) to keep the sample under inert atmosphere. The container was partially immersed in a sand bath on a hot plate with a thermocouple inserted into the sand for heating.

Magnetic characterization

Magnetization measurements were performed using a Quantum Design Physical Properties Measurement System. Samples were prepared by tightly wrapping 25–50 mg of powder in minimal plastic wrap, which was secured in a plastic drinking straw for measurement. DC magnetization measurements were carried out from ~2 K to 300 K in applied DC magnetic fields ($\mu_0 H$) of up to 9 T. Alternating current magnetic susceptibility measurements were carried out under a 0.5 mT alternating current magnetic field at different frequencies, with zero DC magnetic field applied. Heat capacity measurements were performed using the Physical Properties Measurement System on pressed pellets of neat powder or on a collection of dozens of small single crystals, which were affixed to a sapphire platform using Apiezon-N grease. The contribution of the sample holder with grease was subtracted after measuring it separately. Heat capacity was normalized to the sample mass.

Other techniques

Powder XRD patterns were obtained using a Bruker D8 Advance diffractometer equipped with a Cu anode, fixed divergence slits with a nickel filter and a LYNXEYE detector. The instrument was operated in a Bragg–Brentano geometry with a step size of 0.02° (2θ) or less. The simulated powder XRD patterns were calculated using crystallographic information files from single-crystal XRD solutions. The powder XRD of **Au_Cl** was extracted from the PDF dataset using a wavelength of 0.2115 Å and a sample-to-detector distance of 150 cm. Thermogravimetric analysis was performed on a Netzsch TG 209 F1 Libra Thermo-Microbalance with alumina pans at a heating rate of 1 °C min^{-1}. Raman spectra were collected using a Renishaw RM1000 Raman microscope with a 514 nm laser with a power between 0.1 mW and 1 mW and a ~5 µm spot size on powder samples. Differential scanning calorimetry measurements used a TA Instruments Q2500 differential scanning calorimeter using standard aluminium pans and a heating and cooling rate of 5 °C min^{-1}.

Computational methods

We performed DFT calculations using the HSE[42] range-separated hybrid functional using the VASP[43] software. HSE parameters: $\alpha = 0.25$ and $\omega = 0.2$. We used a plane-wave basis with an energy cut-off of 500 eV, and we sampled the Brillouin zone with a 4 × 4 × 4 k-grid. We included 19 valence electrons for Au, 9 for Cs and 7 for Cl in our projector-augmented wave[56] pseudopotentials. Unless otherwise noted, figures were generated using ionic coordinates relaxed with DFT–HSE, started from the structure obtained via single-crystal XRD. The primitive cell vectors determined from single-crystal XRD were: $a = (-x, x, y)$; $b = (x, -x, y)$; and $c = (x, x, -y)$ with $x = 10.485250$ Å and $y = 10.647400$ Å. The space group was $I4_1cd$ (number 110). Our primitive cell included 24 Au atoms, 96 Cl atoms and 32 Cs atoms. After relaxing the structure, we obtained: $x = 10.68$ Å and $y = 10.85$ Å. To reduce computation time, we initially relaxed the structure with a reduced k-grid for the Fock operator (NKRED 2 setting in VASP). Starting from the resulting coordinates, we then relaxed the structure again using the full k-grid. The Wigner–Seitz radii used by VASP in the calculations of the magnetic moment per atom and partial densities of states were as follows (in Å): 1.376 (Au), 1.005 (Cl) and 1.482 (Cs).

Data availability

All the data underlying the findings of this study are available in this article and its Supplementary Information. The crystallographic data for the structures reported in this article have been deposited at the Cambridge Crystallographic Data Centre under deposition numbers CCDC 2164336 (**Cu_Cl** @ 300 K), 2164337 (**Au_Cl** @ 300 K), 2164338 (**Pd_Cl** @ 300 K), 2164339 (**Au_Cl** @ 100 K), and 2164340 (**Au_Cl** @ 400 K). These data can be obtained free of charge via https://www.ccdc.cam.ac.uk/structures/. Raw images from single-crystal X-ray diffraction collections are available from the corresponding author upon reasonable request. Source data are provided with this paper.

References

51. Kraus, F. Caesium tetrachlorido aurate(III), $CsAuCl_4$. *Z. Naturforsch. B* **66**, 871–872 (2011).
52. Zheng, Z.-R., Evans, D. H. & Nelsen, S. F. Studies of the anodic oxidation of 1,4-diazabicyclo[2.2.2]octane. Reactions of the radical cation. *J. Org. Chem.* **65**, 1793–1798 (2000).
53. Wells, H. L. Some complex chlorides containing gold. III. A new cesium-auric chloride. *Am. J. Sci.* **3**, 414 (1922).
54. Wells, H. L., Wheeler, H. L. & Penfield, S. L. On the caesium and rubidium chloraurates and bromaurates; with their crystallography. *Am. J. Sci.* **44**, 157 (1892).
55. Brauer, G. & Sleater, G. Preparation of mixed valent aurate halides. *J. Less-Common Met.* **21**, 283–291 (1970).
56. Blöchl, P. E. Projector augmented-wave method. *Phys. Rev. B* **50**, 17953–17979 (1994).

Acknowledgements
This research was funded by the US National Science Foundation (DMR2102306). K.P.L. was supported by the Center for Molecular Analysis and Design (CMAD) at Stanford University and the Stanford Department of Chemistry William S. Johnson award. C.R.D was supported by a CMAD fellowship. A.J.H. was supported by the Anne T. and Robert M. Bass Stanford Graduate Fellowship. All calculations were supported by the Theory FWP at the Lawrence Berkeley National Laboratory, funded by the US Department of Energy, Office of Science, Basic Energy Sciences, Materials Sciences and Engineering Division, under contract no. DE-AC02-05CH11231. Computations were performed at the National Energy Research Scientific Computing Center, a US Department of Energy Office of Science User Facility located at Lawrence Berkeley National Laboratory, also operated under contract no. DE-AC02-05CH11231. We thank S. J. Teat at Lawrence Berkeley National Laboratory for assistance with crystallography, A. Sica and J. Caram at the University of California Los Angeles for low-energy UV–vis–NIR spectroscopy measurements, and M. Brueggemeyer at Stanford University for additional assistance with EPR measurements. Single-crystal XRD studies were performed at beamline 12.2.1 at the Advanced Light Source at Lawrence Berkeley National Laboratory. Additional single-crystal XRD studies were performed at the Stanford Nanocharacterization Laboratory and differential scanning calorimetry studies were performed at the Soft and Hybrid Materials Facility, both part of the Stanford Nano Shared Facilities, supported by the National Science Foundation under award ECCS-1542152. XAS studies used beamlines 4-1 and 4-3 at Stanford Synchrotron Radiation Lightsource at the SLAC National Accelerator Laboratory. X-ray PDF studies used beamline 11-ID-B at the Advanced Photon Source, a US Department of Energy Office of Science User Facility operated for the Department of Energy Office of Science by Argonne National Laboratory under contract no. DE-AC02-06CH11357. Financial support for D.H.R. was provided by Fonds Quebecois de la Recherche sur la Nature et les Technologies and the Natural Sciences and Engineering Research Council Canada. The ^{197}Au Mössbauer source was prepared in the McMaster Nuclear Reactor, Hamilton Ontario, and the assistance of R. Pasuta is gratefully acknowledged. The funders had no role in study design, data collection and analysis, decision to publish or preparation of the manuscript.

Author contributions
K.P.L. synthesized and characterized the materials. C.R.D. further developed the synthesis and studied the reaction mechanism. A.E., A.G.S. and J.B.N. performed the electronic structure calculations. A.J.H., K.P.L. and E.I.S performed the EPR measurements and analysis. J.W. and Y.S.L. performed the magnetic measurements and analysis. D.H.R. performed the Mössbauer measurements and analysis. H.I.K. defined and guided the project direction. The manuscript was written by K.P.L. and H.I.K with contributions from all authors.

Competing interests
The authors declare no competing interests.

Additional information
Extended data is available for this paper at https://doi.org/10.1038/s41557-023-01305-y.

Supplementary information The online version contains supplementary material available at https://doi.org/10.1038/s41557-023-01305-y.

Correspondence and requests for materials should be addressed to Hemamala I. Karunadasa.

Peer review information *Nature Chemistry* thanks Graeme Blake and the other, anonymous, reviewer(s) for their contribution to the peer review of this work.

https://doi.org/10.1038/s41557-023-01305-y

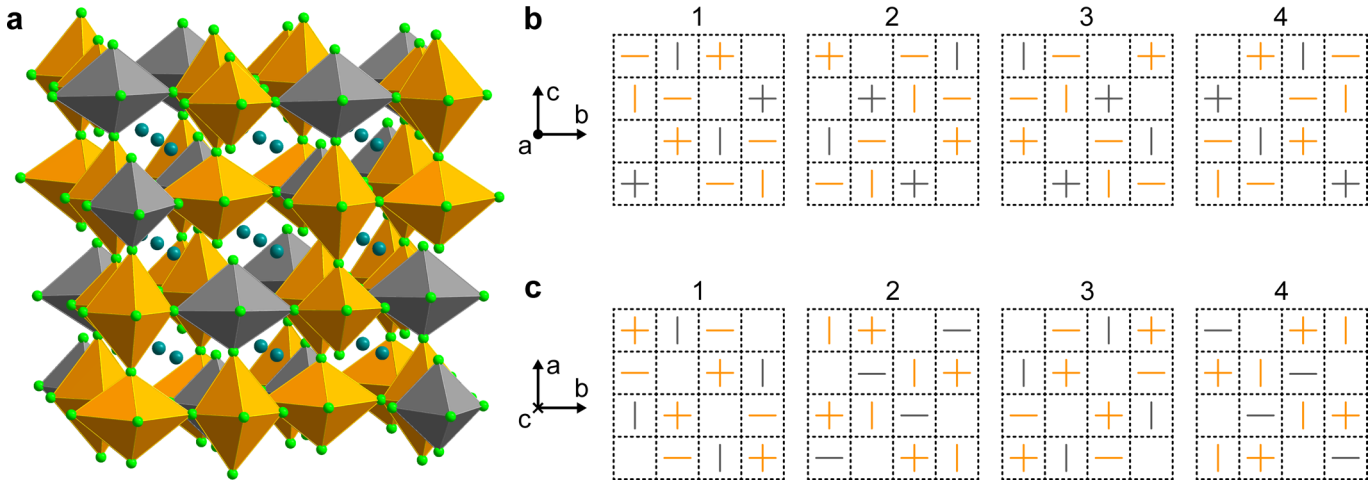

Extended Data Fig. 1 | Representation of the X-ray diffraction single-crystal structure of Pd_Cl. a, A 3D representation where turquoise and light green spheres represent Cs and Cl atoms, respectively, and gold and grey octahedra represent $Au^{III}Cl_6$ and $Pd^{II}Cl_6$, respectively, and the viewing direction is shown by the coordinate system in panel (**b**). **b**,**c**, 2D representations of the crystal structure of **Pd_Cl** where the short, equatorial bonds of the axially elongated $Au^{III}Cl_6$ and $Pd^{II}Cl_6$ octahedra are represented by gold and grey lines, respectively. Equatorial bonds perpendicular to the plane are not drawn. The numbers represent the stacking sequence of the layers along the *a* axis for (**b**) and the *c* axis for (**c**). The structure is isostructral with that of **Au_Cl**. Note: the Au and Pd atoms are partially disordered with respect to one another in the crystal structure, though they still exhibit clear preferences for particular crystallographic sites, which are shown in this figure.

https://doi.org/10.1038/s41557-023-01305-y

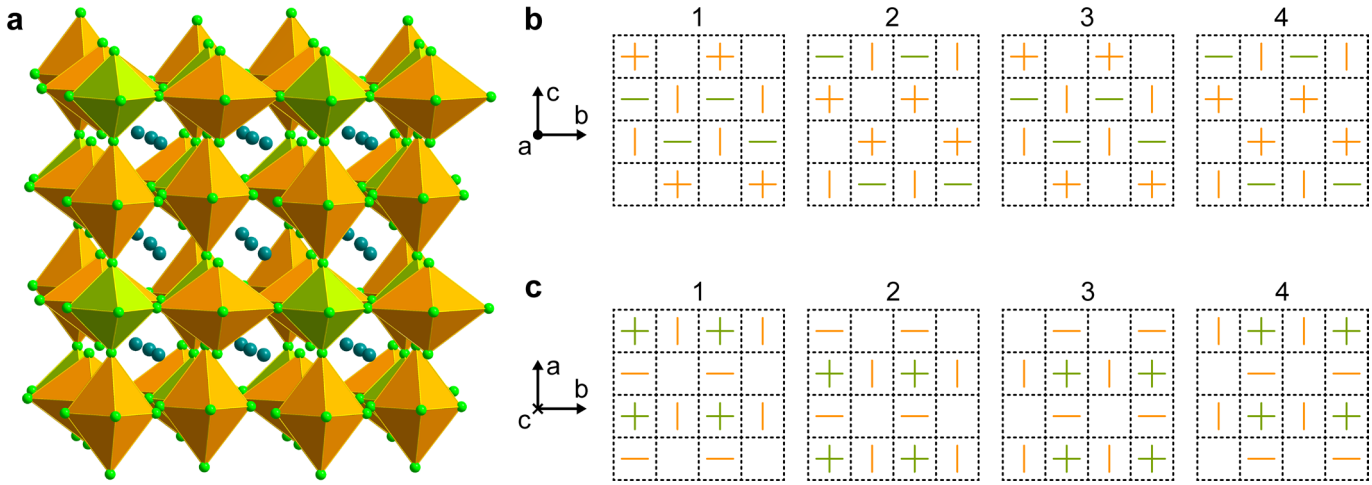

Extended Data Fig. 2 | Representation of the single-crystal structure of Cu_Cl. a, A 3D representation where turquoise and light green spheres represent Cs and Cl atoms, respectively, and gold and green octahedra represent $Au^{III}Cl_6$ and $Cu^{II}Cl_6$, respectively, and the viewing direction is shown by the coordinate system in panel (**b**). **b**,**c**, 2D representations of the crystal structure of **Cu_Cl** where the short, equatorial bonds of the axially elongated $Au^{III}Cl_6$ and $Cu^{II}Cl_6$ octahedra are represented by gold and green lines, respectively. Equatorial bonds perpendicular to the plane are not drawn. The numbers represent the stacking sequence of the layers along the *a* axis for (**b**) and the *c* axis for (**c**). The structure is similar to that of **Au_Cl**, but with a different ordering of the Au^{3+}/B^{2+} and vacancies with respect to one another.

https://doi.org/10.1038/s41557-023-01305-y

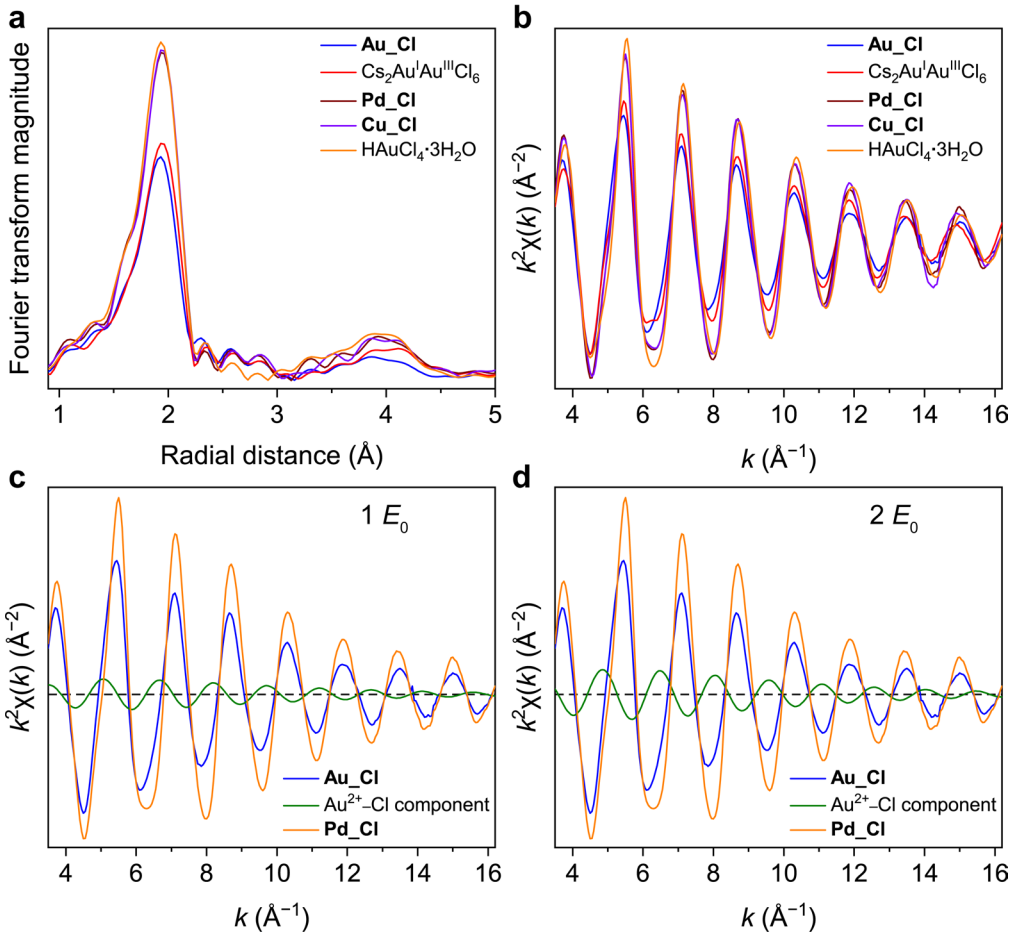

Extended Data Fig. 3 | EXAFS data at the Au L_3 edge. a–d, Data are plotted in *k* space (**b**–**d**) and Fourier transformed to real space (**a**), all with a *k* weight of 2. **c**,**d**, EXAFS data at the Au L_3 edge for **Au_Cl** and **Pd_Cl** and fitted Au^{2+}–Cl component for **Au_Cl**. The text at the top of each plot denotes the number of independent photoelectron threshold energies (E_0) used for the fit to obtain the Au^{2+}–Cl component. The dashed line is placed at $y = 0$ to examine the zero crossing of each wave: the zero crossings for **Au_Cl** are at lower values of *k* than for **Pd_Cl**, particularly in the low-*k* range (~ 4 to 8 *k*), consistent with the presence of the Au^{2+}–Cl component that is offset from the Au^{3+}–Cl component due to the difference in bond length and/or photoelectron threshold energy. See Methods and Supplementary Information for a detailed discussion.

https://doi.org/10.1038/s41557-023-01305-y

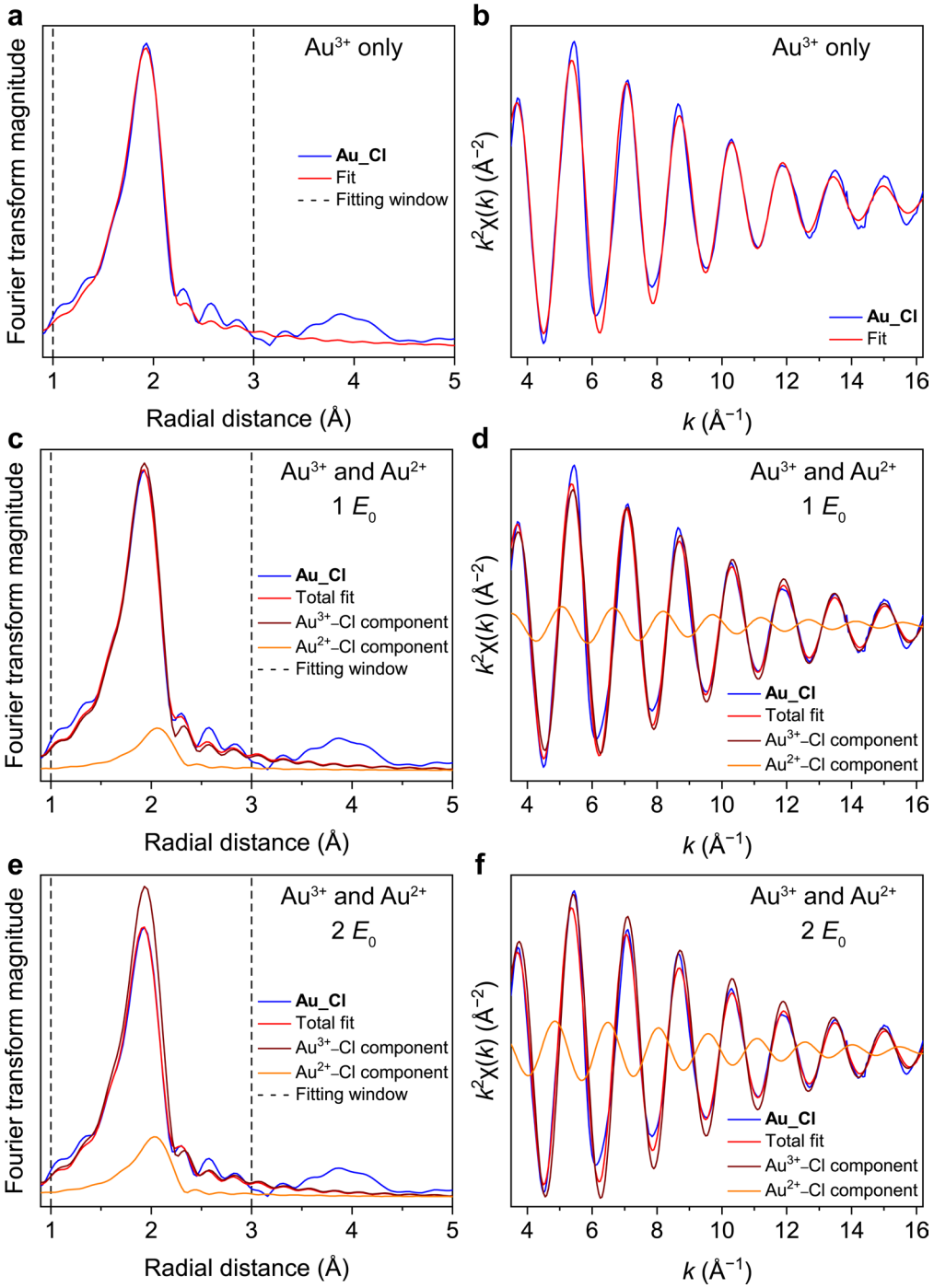

Extended Data Fig. 4 | EXAFS data and fits at the Au L_3 edge for Au_Cl. a–**f**, Data are plotted in *k* space (**b**,**d**,**f**) and Fourier transformed to real space (**a**,**c**,**e**), all with a *k* weight of 2. The text at the top of each plot denotes the parameters used for the fit. The best fit is shown in panels (**c**,**d**), which incorporates both Au^{2+} and Au^{3+} with one independent photoelectron threshold energy. See Methods and Supplementary Information for a detailed discussion and Supplementary Table 7 for fitting results.

https://doi.org/10.1038/s41557-023-01305-y

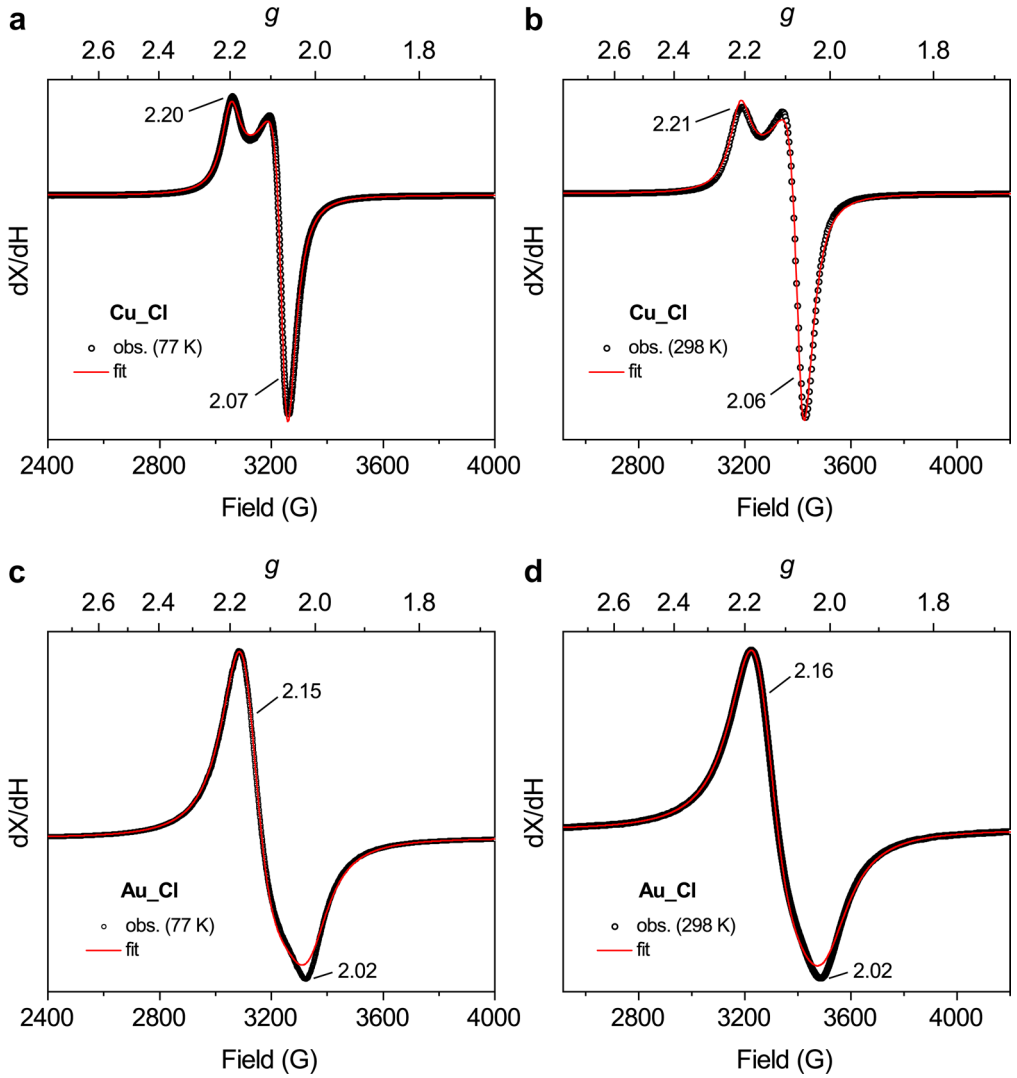

Extended Data Fig. 5 | X-band EPR spectra and fits of Cu_Cl and Au_Cl. a–**d**, Spectra and fits at 77 K (**a**,**c**) and spectra and fits at 298 K (**b**,**d**). The results confirm the oxidation-state assignments of Au in **Au_Cl**. See Methods and Supplementary Information for details about the fitting and quantification and Supplementary Table 8 for fitting results.

https://doi.org/10.1038/s41557-023-01305-y

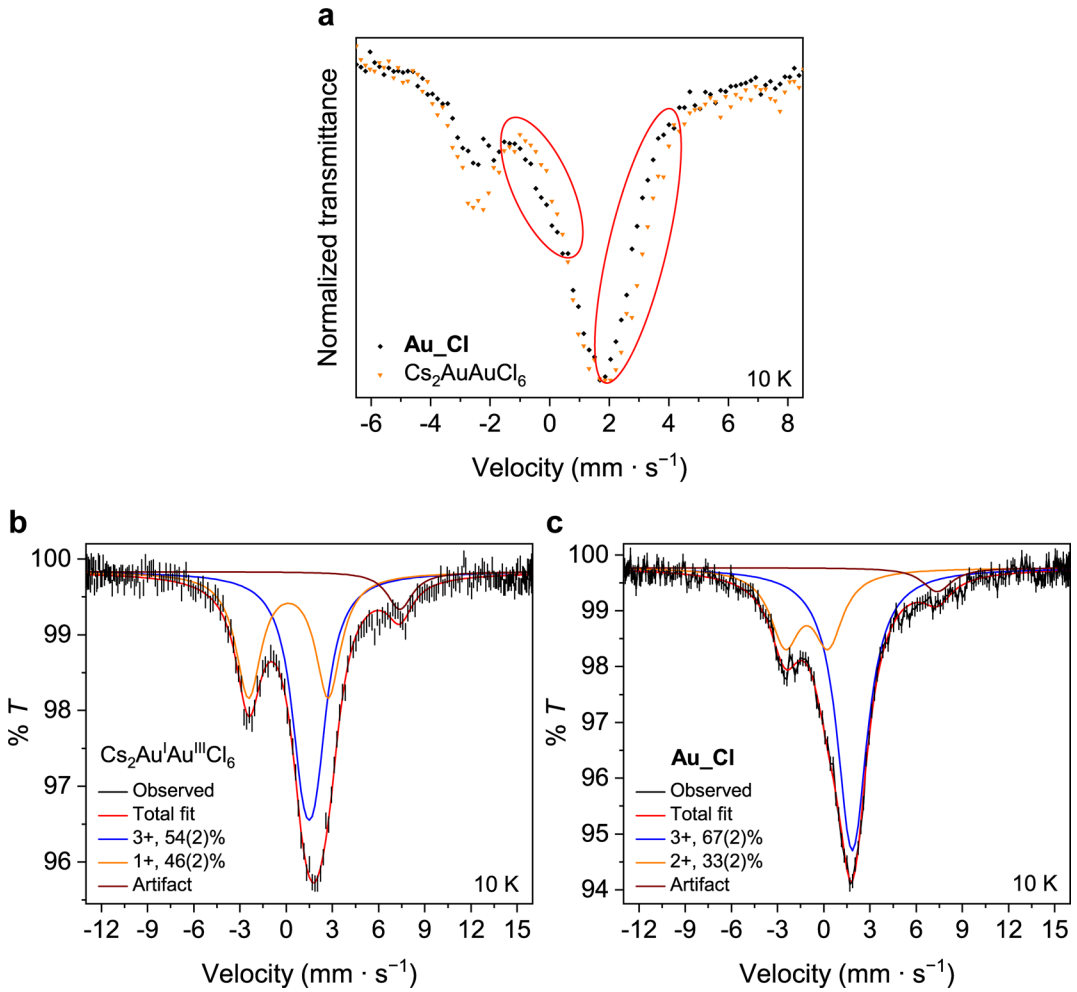

Extended Data Fig. 6 | ^{197}Au Mössbauer spectra collected at 10 K, referenced to a Au° foil. a, Overlayed spectra of **Au_Cl** and $Cs_2Au^{I}Au^{III}Cl_6$, with the red ellipses highlighting the differences between the two spectra that correspond to the replacement of Au^{1+} with Au^{2+}. **b**, The best fit to the spectrum of $Cs_2Au^{I}Au^{III}Cl_6$. **c**, The best fit to the spectrum of **Au_Cl**. The Au^{3+} doublets are unresolved due to their small values of quadrupole splitting. The observed data in (**b**) and (**c**) are plotted as vertical bars representing the measurement uncertainty (1σ). The results confirm the oxidation-state assignments of Au in **Au_Cl**. See Methods and Supplementary Information for details about the fitting, Extended Data Table 1 for fitting results, and Supplementary Table 9 for literature values.

https://doi.org/10.1038/s41557-023-01305-y

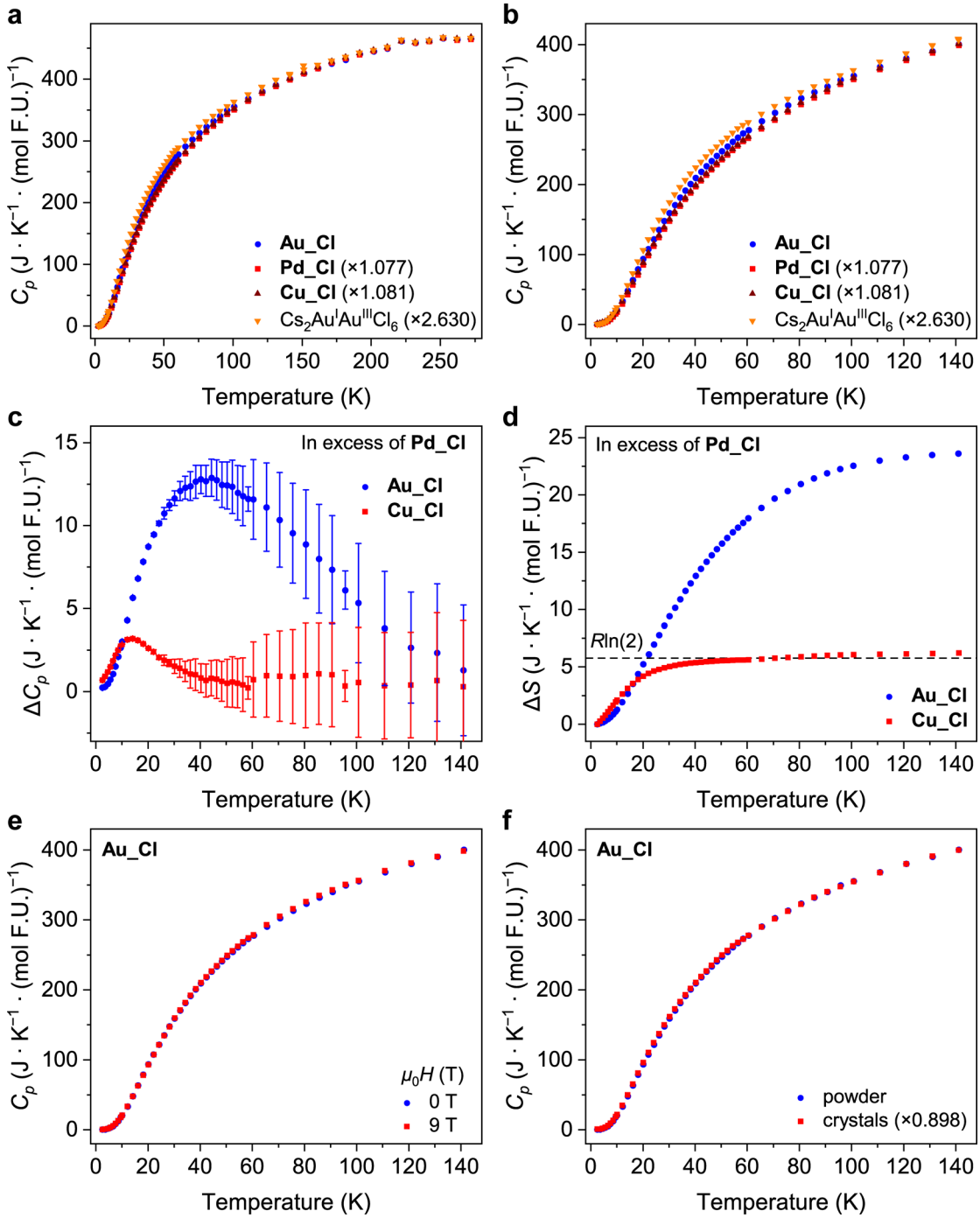

Extended Data Fig. 7 | Heat capacity measurements. a, Heat capacity normalized at high temperatures (~ 200–275 K). **b**, A magnified region of the same data presented in (**a**). The scaling factors denoted in the legends in (**a**,**b**) are probably due to inaccuracies in the measured sample masses and are scaled with respect to **Au_Cl**. **c**, The heat capacity in excess of that of **Pd_Cl**. The vertical bars represent the measurement uncertainty (1σ). **d**, Entropy (ΔS) as extracted from the heat capacity in excess of that of **Pd_Cl**. The dashed horizontal line at $R\ln(2)$ represents the expected excess entropy for a magnetic centre with spin $S = 1/2$. **e**, Heat capacity of **Au_Cl** with no applied magnetic field as compared to that in an applied magnetic field of 9 T, showing no meaningful change. **f**, Heat capacity of single crystals and a pressed pellet of **Au_Cl** powder. The scaling factor is an estimate due to the difficulty in obtaining an accurate mass of the crystals used for the measurement. The error bars in (**a**,**b**,**e**,**f**) are smaller than the points as drawn and were therefore not included in the figures. The results show an intriguing excess of magnetic entropy for **Au_Cl** beyond the expected value for a system with $S = 1/2$.

https://doi.org/10.1038/s41557-023-01305-y

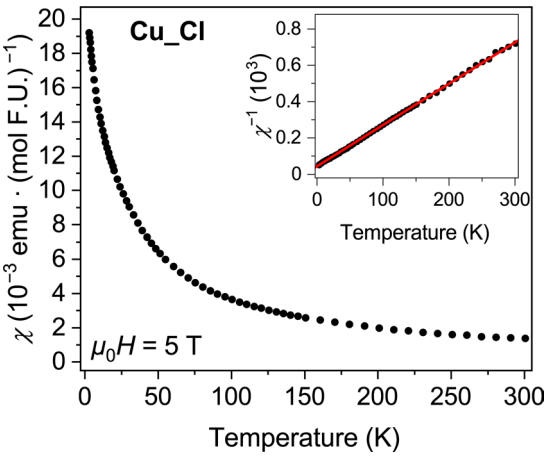

Extended Data Fig. 8 | Magnetic characterization of Cu_Cl. Magnetic susceptibility (χ) from DC magnetization data with χ versus temperature at a single applied field (μ_0H) and with a diamagnetic correction $\chi_0 = 2.25 \times 10^{-3}$ emu · (mol F.U.)$^{-1}$, where F.U. = formula unit and 1 emu · (mol Oe)$^{-1}$ = (4π)10^{-6} m^3 · mol^{-1}. The inset shows the inverse susceptibility data with a Curie–Weiss fit (red line) from 50 to 200 K. The results indicate weak antiferromagnetic interactions. See Methods and Supplementary Information for details about the fitting and Supplementary Table 10 for fitting results.

https://doi.org/10.1038/s41557-023-01305-y

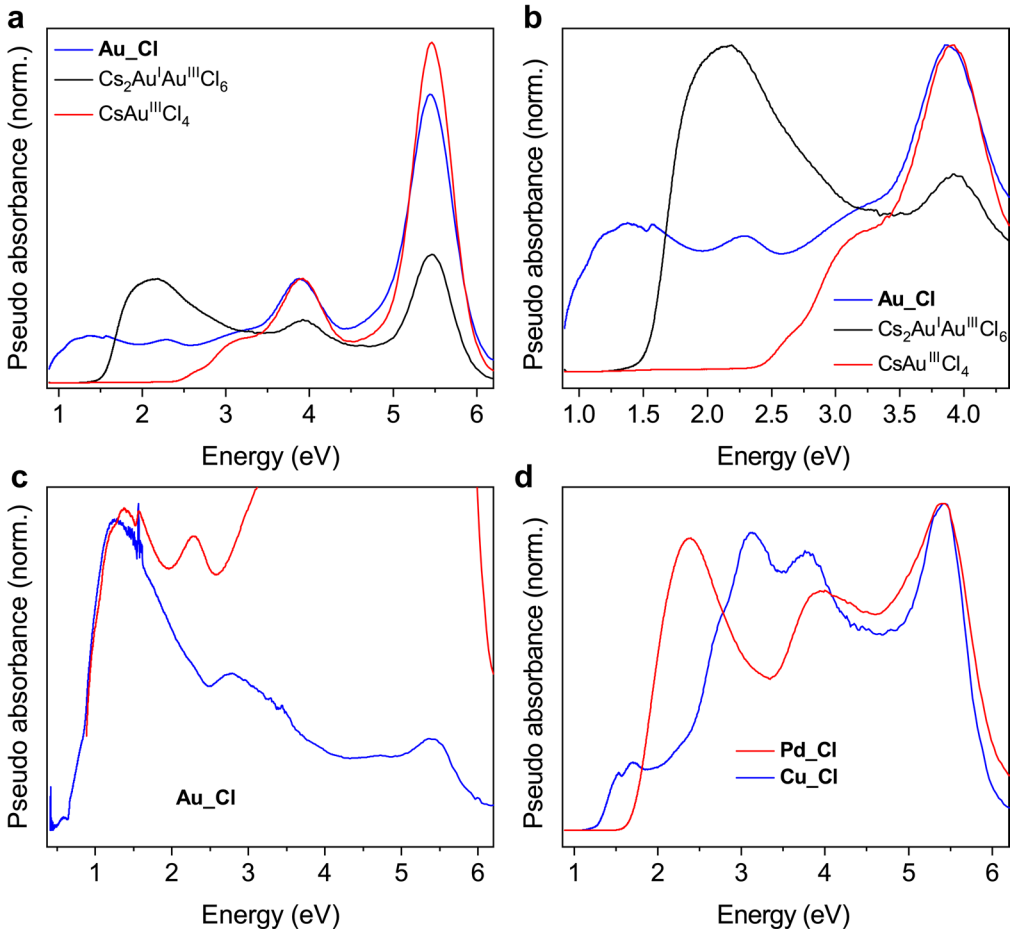

Extended Data Fig. 9 | UV–vis–NIR absorbance spectra of crystals pulverized into a mull with $BaSO_4$ and converted from diffuse reflectance spectra using the Kubelka–Munk transformation. a,**b**,**d** Spectra normalized to the highest point at or below 4.5 eV. **c**, Spectra normalized to align near the first absorption peak. The same spectra are shown in (**a**) and (**b**) with two different energy axis ranges for clarity. The two spectra in (**c**) were collected with two different spectrophotometers to acquire a larger energy range. The low-energy absorption onset for **Au_Cl** is probably due to a low-energy $Au^{2+/3+}$ intervalence charge transfer. See Methods and Supplementary Information for a detailed discussion.

https://doi.org/10.1038/s41557-023-01305-y

Extended Data Table 1 | ^{197}Au Mössbauer fit results

Sample	3+ doublet			2+/1+ doublet			FWHM	Reduced χ^2
	IS	QS	%	IS	QS	%		
Au_Cl	1.85(2)	0.3(2)	67(2)	−1.11(6)	2.80(9)	33(2)	2.31(8)	1.01
$Cs_2Au^{I}Au^{III}Cl_6$	1.49(2)	0.79(6)	54(2)	0.14(3)	5.17(5)	46(2)	1.99(5)	0.96

The results confirm the oxidation-state assignments of Au in **Au_Cl**. All values are referenced to a Au° foil and are in mm · s^{-1} unless otherwise noted. All data were collected at 10 K. See Methods and Supplementary Information for details about the fitting, Extended Data Fig. 6 for the plotted ^{197}Au Mössbauer data and fits, and Supplementary Table 9 for literature values.